

# Self-aligned optical microcomb emerging between octave separated lasers

Grégoire Moille,<sup>1,2,\*</sup> Pradyoth Shandilya,<sup>3</sup> Jordan Stone,<sup>2</sup> River Beard,<sup>4</sup> Shao-Chien Ou,<sup>1,2</sup>

Zongda Li,<sup>5,6</sup> Mark Harrington,<sup>7</sup> Kaikai Liu,<sup>7</sup> Robert Rockmore,<sup>8</sup> Curtis R. Menyuk,<sup>3</sup>

Daniel J. Blumenthal,<sup>7</sup> Sean P. Krzyzewski,<sup>8</sup> Miro Erkintalo,<sup>5,6</sup> and Kartik Srinivasan<sup>1,2,†</sup>

<sup>1</sup>Joint Quantum Institute, NIST/University of Maryland, College Park, USA

<sup>2</sup>Microsystems and Nanotechnology Division, National Institute of Standards and Technology, Gaithersburg, USA

<sup>3</sup>University of Maryland Baltimore County, Baltimore, MD, USA

<sup>4</sup>AV Incorporated, Albuquerque, New Mexico, USA

<sup>5</sup>Department of Physics, University of Auckland, Auckland 1010, New Zealand

<sup>6</sup>The Dodd-Walls Centre for Photonic and Quantum Technologies, New Zealand

<sup>7</sup>Department of Electrical and Computer Engineering, University of California Santa Barbara, Santa Barbara, CA, USA

<sup>8</sup>Air Force Research Laboratory, Space Vehicles Directorate, Kirtland Air Force Base 87117, USA

(Dated: February 9, 2026)

Optical frequency combs (OFCs) are frequency rulers essential for precision metrology, next generation navigation, and testing of fundamental physics.<sup>1</sup> Despite intense efforts, chip-integrated OFCs remain laboratory-bound, unable to fulfill their promise of compact and cost-effective deployment. While improvement in fabrication and integration are important, a conceptual limitation has fundamentally stymied progress: on-chip OFC architectures have aimed to miniaturize their table-top counterparts and relied on cascading outward from (i.e., spectrally broadening) a single pump.<sup>2,3</sup> In integrated platforms, this approach does not readily allow for the generation of strong and low-noise octave-spaced signals that are crucially needed for robust zero-frequency offset detection.<sup>4</sup> Here, we overcome this limitation via an architectural inversion where an optical microcomb forms by filling the spectrum between two octave-separated pump lasers. The two pumps generate a parametrically driven cavity soliton (PDCS)<sup>5</sup> in an integrated  $\chi^{(3)}$  resonator,<sup>6</sup> which robustly self-aligns to (i.e., synchronizes with) the pump lasers across multiple foundry-fabricated devices and operating configurations. This produces a single octave-spanning comb extending from telecom to visible wavelengths, whose zero-frequency offset is completely defined by the two harmonically-related pump lasers, and can therefore be reliably detected and stabilized. We showcase our platform's capabilities by executing all of the three core tasks of OFC metrology: optical frequency synthesis, low-noise millimeter-wave generation, and integrated optical clock readout, using the same self-aligned microcomb with only its input locks changed.

Ultra-precise optical frequency measurement and stabilization enables positioning, navigation, and timing beyond GPS,<sup>7</sup> quantum computing,<sup>8</sup> quantum sensing,<sup>9</sup> fundamental physics measurements,<sup>10,11</sup> and may redefine the second.<sup>12,13</sup> Optical frequency combs (OFCs)—optical frequency rulers with evenly spaced markers and a known zero-frequency offset<sup>1</sup>—are a key enabling technology for these applications, providing a coherent optical to microwave two-way link for ultra-high precision optical frequency measurement,<sup>14</sup> synthesis,<sup>15</sup> and ultra-low noise microwave generation.<sup>16</sup> Reducing the size, weight, power, and cost (SWaP-C) of OFCs through mass-scale fabrication can enable field deployment and lab-to-consumer transition along with the critical technologies they empower. This vision has driven significant efforts to generate OFCs in integrated photonics platforms.

Miniaturizing from the table top to the chip-scale, integrated OFCs also relies on using the second ( $\chi^{(2)}$ ) or third ( $\chi^{(3)}$ ) order optical nonlinearity to spectrally broaden a narrowband input to obtain evenly spaced comb teeth

spanning an octave,<sup>17–20</sup> thus enabling  $\nu - 2\nu$  nonlinear interferometry to measure and stabilize the comb's carrier-envelope offset (CEO).<sup>21,22</sup> Dissipative Kerr solitons (DKSs) in on-chip microresonators<sup>2</sup> constitute a particular system of interest that leverages the photonic material's  $\chi^{(3)}$  nonlinearity as an ultra-broadband gain medium. Generated from a continuous wave (CW) pump laser, chip-integrated DKS combs can span an octave<sup>3</sup> and are compatible with mass-scale foundry fabrication<sup>23,24</sup> and low power consumption.<sup>25</sup> However, while DKS combs have proven their effectiveness in numerous applications,<sup>1,2,26</sup> the fact that they form by cascading outward from a low-power seed pump laser leads to fundamental limitations for metrology applications: Octave-spaced signals at the comb edges are typically very weak and noisy (due to thermo-refractive fluctuations<sup>4</sup>), which critically hinders the detection and stabilization of the CEO. These limitations have restricted precise predictability of the DKS repetition rate,<sup>27</sup> and direct CEO detection and locking, to a small handful of laboratory demonstrations<sup>4,28–33</sup> that often involve complex apparatuses and/or additional helper lasers, limiting deployable integrated frequency metrology.

In this work, we demonstrate a new paradigm for integrated OFC generation and self-referencing that overcomes current limitations. Fundamentally departing

\* gmoille@umd.edu

† kartik.srinivasan@nist.gov

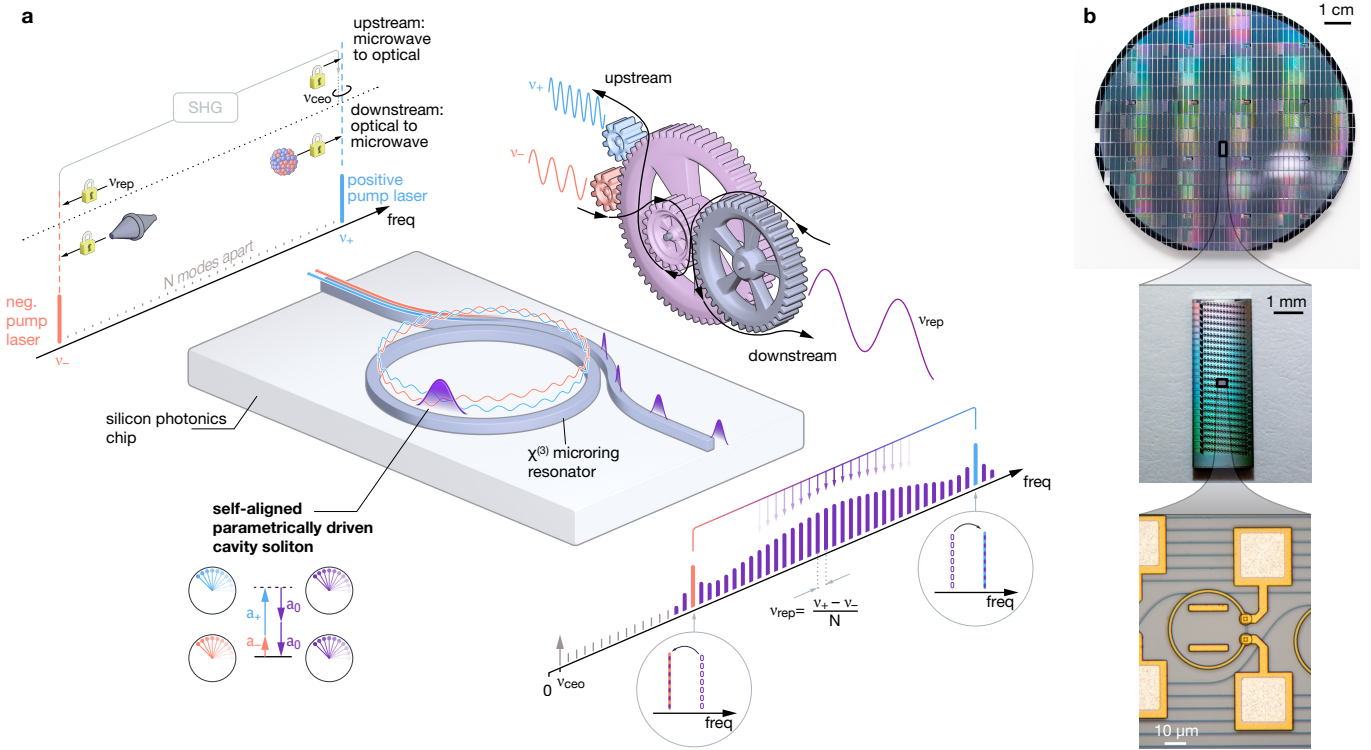


**Fig. 1 – Concept of self-aligned parametrically driven cavity soliton (PDCS) microcomb generation with octave-separated lasers** **a**, Schematic of dual-pump PDCS generation. Two pump lasers (with frequencies  $\nu_-$  and  $\nu_+ \approx 2\nu_-$ ) are injected into a  $\chi^{(3)}$  microring resonator where they interact nonlinearly to generate a PDCS. By minimizing their phase difference, the Kerr nonlinearity phase-locks all components (lower left inset), leading to the PDCS self-synchronizing to both of the pump fields. The output microcomb spectrally fills the gap between the two pump lasers, with both capturing their nearest PDCS comb teeth to form a unique, single frequency grid. The repetition rate thus becomes deterministic as  $\nu_{\text{rep}}^{\text{pdc}} = (\nu_+ - \nu_-)/N$ , where  $\nu_+$ ,  $\nu_-$ , and  $N$  are all known. Moreover, the quasi-harmonic pump configuration enables carrier-envelope offset (CEO) definition ( $\nu_{\text{ceo}}$ ) and locking prior to comb generation, for complete system self-stabilization, which in turn enables straightforward interfacing with locked lasers and microwave sources for core OFC tasks in both the microwave and optical domains. **b**, Photographs (top and center) and micrographs (bottom) of the 100 mm foundry-fabricated silicon nitride wafer (see Methods) in which our new deployable microcomb architecture is demonstrated.

from conventional comb generation architectures that rely on cascading outwards from a single pump, our concept is underpinned by recently-discovered parametrically driven cavity solitons (PDCSs)<sup>5</sup> that can manifest themselves in  $\chi^{(3)}$  resonators driven by two CW pump lasers.<sup>6</sup> Such PDCSs correspond to frequency combs that are centred in between the two pumps, and exhibit characteristics that make them potentially attractive for a variety of applications, such as those described in this work. Here, we report on two transformative advances in integrated  $\chi^{(3)}$  PDCS generation that underline their direct potential for comb metrology: (i) the ability to generate on-chip PDCS combs with two octave-separated pumps, and (ii) the possibility that a generated PDCS comb can nonlinearly align itself with the pumps (in a manner reminiscent of Kerr-induced synchronization of conventional DKSs<sup>34</sup>) resulting in a single frequency grid across the entire pump span. These advances—which are robust and can be realized in multiple foundry-fabricated devices and pump configurations—allow us to produce a single, octave-spanning OFC spanning telecom to visible wavelengths with intrinsic two-point microcomb stabilization control. Crucially, because the octave-separated

pumps are both comb lines (when operating in the self-alignment regime), the CEO of the subsequently generated PDCS is *a priori* determined before the chip from the harmonic relationship between both pumps, enabling tremendous flexibility in interfacing the comb with microwave and optical frequency references. We show that by simply changing how the input lasers are locked, the same self-aligned PDCS can perform all of the three core tasks associated with self-referenced OFCs: synthesizing optical frequencies from known microwave frequencies, generating low-noise micro/millimeter waves from low-noise lasers, and generating a stable microwave timing signal from an atomically-referenced laser.

## Concept and experimental demonstration

Our system begins with a chip-integrated  $\chi^{(3)}$  microring resonator (Fig. 1a). Instead of driving the resonator with a single pump that cascades outward to generate a conventional DKS microcomb, we use two pumps at frequencies  $\nu_{\pm}$  and resonator azimuthal modes  $n_{\pm}$ , respectively. Under conditions where the resonator dispersion allows for phase- and frequency-matching of the degenerate four-wave mixing process  $\nu_+ + \nu_- = 2\nu_0$ , and where

the parametric signal frequency  $\nu_0 = (\nu_+ + \nu_-)/2$  experiences anomalous group-velocity dispersion, a broadband PDCS comb can be generated and sustained around the signal frequency  $\nu_0$ .<sup>6</sup>

Inside the resonator, the PDCS nonlinearly interacts with the fields at the pump frequencies  $\nu_{\pm}$  to produce frequency combs around those pumps. The Kerr-nonlinearity locks the group velocities of the PDCS and pump combs so that they are identical, yielding identical repetition rates (comb line spacings). However, because the fields at  $\nu_{\pm}$  and  $\nu_0$  in general exhibit different phase-velocities, the combs possess different CEO frequencies.<sup>35</sup> Thus, the output microcomb in general consists of three distinct frequency grids: the central PDCS and one around each of the pump lasers. All three grids have the same repetition rate  $\nu_{\text{rep}}$ , but they are offset from one another by a frequency  $-\Delta\nu_{\text{ceo}}$  between the  $\nu_-$  grid and the PDCS and  $\Delta\nu_{\text{ceo}}$  between the PDCS and the  $\nu_+$  grid.

The metrological uses of PDCS combs may appear limited because they do not in general form a single frequency grid, instead exhibiting a new degree of freedom ( $\Delta\nu_{\text{ceo}}$ ). Linear theory asserts that the frequency offset  $\Delta\nu_{\text{ceo}}$  is determined by the resonator dispersion and the detunings of the pump lasers.<sup>6</sup> While it is theoretically possible for the PDCS comb to be aligned with the pumps (such that  $\Delta\nu_{\text{ceo}} = 0$ ), reaching and maintaining this set point could be expected to require judicious dispersion engineering and pump detuning stabilization.

Remarkably however, numerical simulations show (see Section S.1) that this expectation described is inaccurate; linear theory does not correctly predict the system behaviour when the frequency offset  $\Delta\nu_{\text{ceo}}$  is small. Our simulations reveal instead that the PDCS can self-align itself with the pump frequencies due to the Kerr nonlinearity, so that  $\Delta\nu_{\text{ceo}} = 0$  over a broad range of parameters (including pump frequencies) when the frequency offsets predicted by linear theory are small. This self-alignment is directly related to the phenomenon of Kerr-induced synchronization that was recently demonstrated for conventional DKSs, where a single comb line of the DKS is captured by (synchronized to) an externally injected laser whose frequency is sufficiently close to the comb line (within a given locking range).<sup>34</sup> Our simulations suggest that, when  $\Delta\nu_{\text{ceo}} \approx 0$ , the two pumps can first generate the PDCS and then capture it, passively locking the frequency offsets  $\Delta\nu_{\text{ceo}}$  exactly at zero to yield a single frequency grid across the entire pump span  $\nu_+ - \nu_-$  (Fig. 1b).

The possibility of PDCS self-alignment is fundamentally interesting as an example of how the Kerr nonlinearity can create phase- and group-coherent patterns; moreover, it has significant ramifications for on-chip metrology applications if the two pumps generating and capturing the PDCS can be engineered to be quasi-harmonically related, i.e.,  $\nu_+ \approx 2\nu_-$  and  $n_+ = 2n_-$ . Because both pumps become part of the PDCS comb, they satisfy  $\nu_+ = 2n_- \nu_{\text{rep}}^{\text{pdc}} + \nu_{\text{ceo}}^{\text{pdc}}$  and  $\nu_- = n_- \nu_{\text{rep}}^{\text{pdc}} + \nu_{\text{ceo}}^{\text{pdc}}$ , highlighting

how the CEO frequency  $\nu_{\text{ceo}}^{\text{pdc}}$  can be readily measured and stabilized before the chip by simply measuring the strong beat between one of the pump lasers ( $\nu_+$ ) and the second-harmonic of the other ( $2\nu_-$ ). This key capability not only allows one to leverage the strength and low noise of the pump lasers to obtain robust CEO stabilization, but it also enables flexible use of the same microcomb in multiple different OFC applications. Before the chip, one can choose a standard two-point microcomb locking architecture<sup>36–38</sup> with locked lasers for microcomb stabilization, or setting the CEO frequency ( $\nu_{\text{ceo}}$ ) for complete self-referencing while maintaining another degree of freedom for repetition rate ( $\nu_{\text{rep}}$ ) stabilization or optical locking to cavity references or atomic clocks.

We demonstrate the above concept experimentally using silicon nitride ( $\text{Si}_3\text{N}_4$ ) microresonator devices obtained via commercial four-inch wafer foundry fabrication (Fig. 1b). Our device geometry consists of 660 nm thick  $\text{Si}_3\text{N}_4$  microring resonators with an outer radius of  $RR = 31 \mu\text{m}$  (free spectral range of  $D_1 \approx 735 \text{ GHz}$ ), ring widths varying from  $RW = 840 \text{ nm}$  to  $RW = 860 \text{ nm}$ , and full  $\text{SiO}_2$  cladding. The rings are coupled to a pulley-like bus waveguide<sup>39</sup> designed to optimize coupling across more than an octave from about 190 THz to 390 THz (see Methods and Supplementary Information for details).

The geometrical dimensions of the microrings are carefully designed so as to engineer the resonator dispersion (Fig. 2a) to simultaneously satisfy the conditions for PDCS existence (phase- and frequency-matching) and its self-alignment to pump lasers separated by an octave. The first requirement is the degenerate optical parametric oscillation (OPO) condition for the creation of the PDCS, resulting in minimization of the frequency mismatch  $2\Delta\nu(n) = [\nu_{\text{res}}(n_+) + \nu_{\text{res}}(n_-)] - [\nu_{\text{res}}(n) + \nu_{\text{res}}(n_+ + n_- - n)]$  at the center mode  $2n_0 = n_- + n_+$  ( $\pm 1$  when  $n_-$  is odd), where  $\nu_{\text{res}}$  are the resonance frequencies and  $n_{\pm}$  are the pumped mode. The second condition, for the self-alignment, requires one to minimize the phase velocity mismatch between the PDCS and its pumps, which is achieved when the PDCS integrated dispersion,  $D_{\text{int}}(n - n_0) = \nu_{\text{res}}(n - n_0) - \left[ \frac{\nu_{\text{res}}(n_+) + \nu_{\text{res}}(n_-)}{2} + D_1(n - n_0) \right]$ , is close to zero at both pumps, and where our definition of  $D_{\text{int}}$  has units of linear and not angular frequency. This minimizes the frequency offsets  $\Delta\nu_{\text{ceo}}$  (small residual offsets can be compensated via pump frequency tuning to reach efficient PDCS self-synchronization). The conditions above essentially reduce to minimizing odd-order dispersion to obtain symmetric PDCS integrated dispersion that crosses zero at the two octave-separated pumps. While this may appear stringent, we have found that coupling engineering—particularly overcoupling of the  $\nu_-$  pump in the C-band—provides sufficient flexibility in pump detuning to allow us to fulfill the conditions across multiple devices (with different ring geometries) and pumped mode pairs (see Section S.5), enabling robust self-aligned PDCS generation.

Figure 2 shows illustrative experimental results of

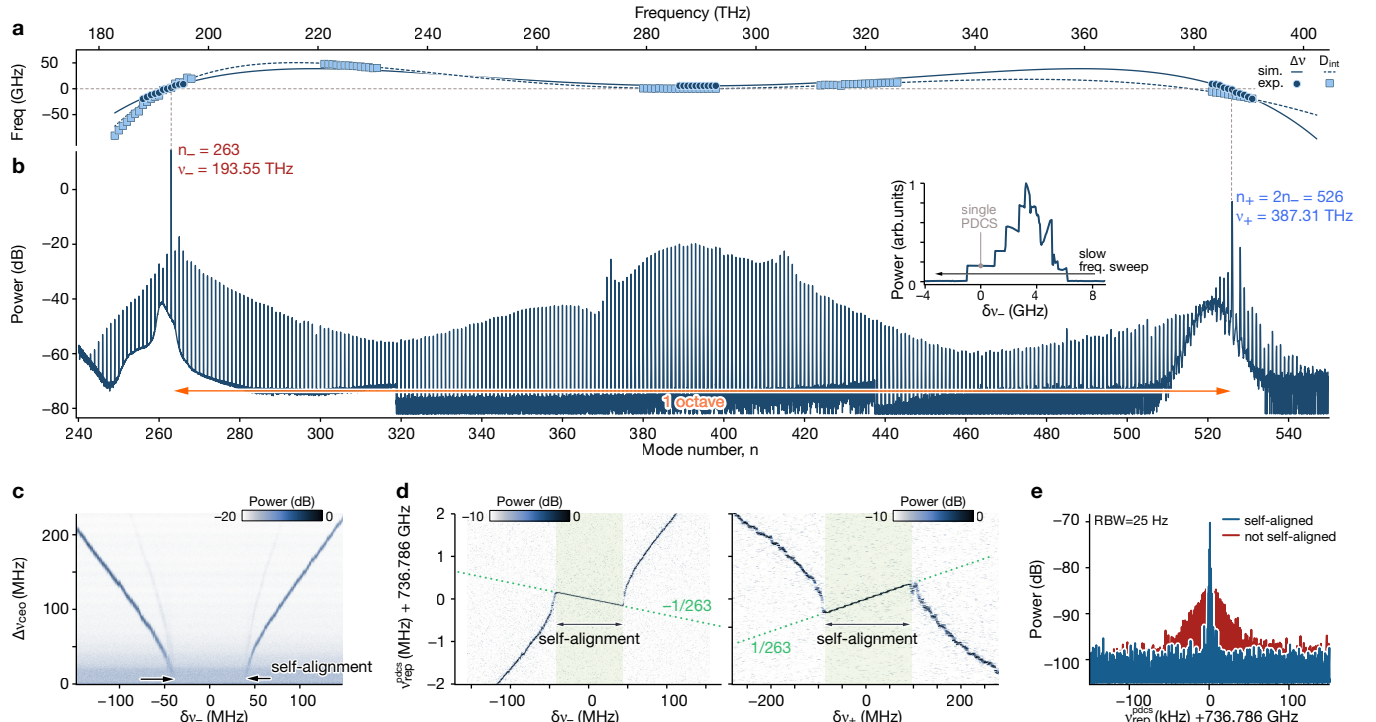


**Fig. 2 – Demonstration of self-aligned octave-spanning PDCS microcomb** **a**, Dispersion engineering for dual-pump PDCS generation ( $RW = 850$  nm). OPO frequency mismatch  $\Delta\nu$  (circles: measured, solid line: simulation) when pumped at  $n_- = 263$  ( $\nu_- = 193.55$  THz) and  $n_+ = 2n_- = 526$  ( $\nu_+ = 387.31$  THz) is minimized at  $2n_0 = n_- + n_+ + 1$ , enabling PDCS generation. Note  $\Delta\nu > 0$  at  $n_0$  since this is a cold-cavity measurement, with  $\Delta\nu$  reduced when driven in the PDCS regime. PDCS integrated dispersion  $D_{\text{int}}(n - n_0)$  (squares: measured, dashed line: simulation) exhibits zero-crossing at both pumps, minimizing their phase offset with respect to the PDCS to enable efficient Kerr-induced synchronization. **b**, Octave-spanning PDCS spectrum demonstrating a gap-free, 220 THz span single frequency grid with all comb teeth above  $-60$  dB. The power is referenced to 1 mW, i.e. equivalent to dBm. Inset: adiabatic PDCS access via pump tuning. **c** Spectrogram from the homodyne detection of the frequency offset  $\Delta\nu_{\text{ceo}}$  between the PDCS and  $\nu_+$  comb components for negative pump frequency detuning  $\delta\nu_-$ .  $\Delta\nu_{\text{ceo}}$  is observed to vanish over a finite range, signaling the formation of a single frequency grid thanks to Kerr induced synchronization of the PDCS to the pumps. **d**, Repetition rate disciplining: once synchronized,  $\nu_{\text{rep}}^{\text{pdc}}$  directly follows optical frequency division set by the pump separation ( $N = 263$ ) and is linearly disciplined against the pump frequency detuning. **e**, Therefore, the synchronization substantially reduces the repetition rate noise compared to the unsynchronized PDCS, detailed in the next section. The power is referenced to 1 mW, i.e. equivalent to dBm.

octave-spanning, self-aligned PDCS microcomb generation in a  $RW = 850$  nm microring. For this device, the dispersion conditions were fulfilled with  $\nu_- \approx 193$  THz ( $n_- = 263$ , C-band) and  $\nu_+ \approx 387$  THz ( $n_+ = 2n_- = 526$ , visible), respectively (Fig. 2a). In the linear regime, the frequency mismatch  $\Delta\nu(n_0) > 0$  is small enough that thermo-optic effects from dual pumping enable  $\Delta\nu(n_0) \approx 0$  to be achieved (see Section S.3).

Using on-chip pump powers of  $P_- = 145$  mW and  $P_+ = 70$  mW for the pumps at  $\nu_-$  and  $\nu_+$ , respectively, we deterministically generate an octave-spanning PDCS [Fig. 2b] through slow frequency tuning of the C-band pump with the visible pump fixed on-resonance (see Methods for further details). This procedure produces a continuous single frequency grid, with all comb teeth between the two octave-separated pump lasers above 1 nW (i.e.,  $-60$  dBm). The dual-pump operation of the PDCS enables thermal compensation for temperature stabilization (see Methods and Supplementary Information S.3), reminiscent of auxiliary pump cooling for standard DKSSs.<sup>40,41</sup> Together with the wafer-scale fabrication by which the devices are created and latitude on

geometric parameters as shown in Supplementary Information S.5, we find the realization of self-aligned octave-spanning PDCSs to be as simple as conventional octave-spanning DKSSs.

To demonstrate self-alignment, we directly measure the frequency offset,  $\Delta\nu_{\text{ceo}}$ , between the PDCS comb and the comb around the  $\nu_+$  pump frequency. To this end, we apply a band-pass filter to isolate spectral components in the 300 THz region, where sufficient power exists for both PDCS and pump comb components (see Section S.6), and obtain  $\Delta\nu_{\text{ceo}}$  by measuring the radio frequency beat signal recorded on a photodetector. By tuning the negative pump frequency  $\nu_-$ , we are able to actuate  $\Delta\nu_{\text{ceo}}$  (Fig. 2c), finding that it vanishes exactly and locks to zero over a finite range of pump frequencies. This observation acts as a telltale sign that the PDCS has self-aligned with the pumps to form a single octave-spanning comb.

In analogy with Kerr-induced synchronization of conventional DKSSs,<sup>34</sup> the repetition rate of a self-aligned PDCS is fully defined by its two pumps, which are part of the comb and act as pinned teeth:  $\nu_{\text{rep}} = (\nu_+ - \nu_-)/(n_+ -$

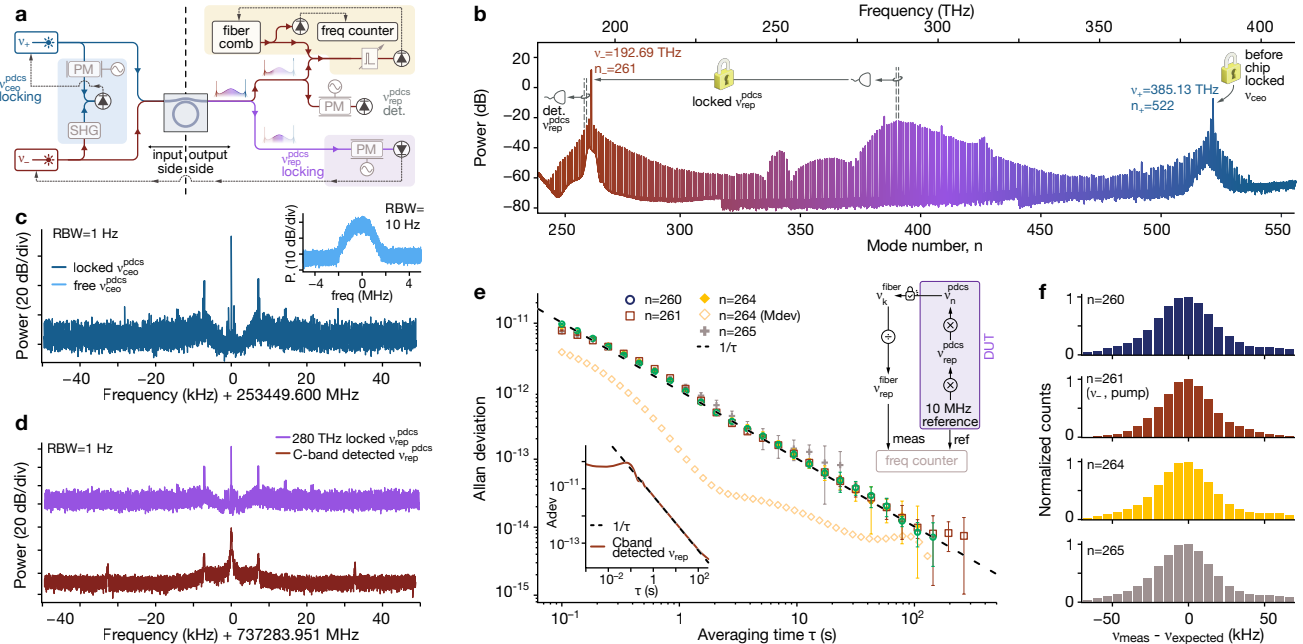


**Fig. 3 – Microwave-to-optical link: self-aligned PDCS self-referencing for optical frequency synthesis**— **a** Simplified experimental setup for optical frequency synthesis using a self-aligned PDCS microcomb. The CEO is set by doubling  $\nu_-$  and beating against  $\nu_+$ , before the chip, with stabilization achieved by feedback onto  $\nu_+$ . An electro-optic comb (EOcomb) apparatus enables operation for a CEO frequency larger than the direct photodetection bandwidth. The  $\nu_-$  pump remains an unused PDCS degree of freedom that is subsequently used in locking the repetition rate  $\nu_{\text{rep}}$ , which is detected in the 280 THz band using another EOcomb apparatus (purple module). Additional detection of  $\nu_{\text{rep}}$  is performed in the C-band (near 190 THz). A fiber OFC, with one comb tooth locked to a selected tooth of the PDCS (yellow module), enables optical frequency counting of the PDCS, which can serve as a backbone for optical frequency synthesis. All locks are referenced to a 10 MHz Rb standard. PM: phase modulator, SHG: second harmonic generation. **b** PDCS spectrum ( $RW = 860$  nm) with harmonic pumps at  $n_- = 261$  and  $n_+ = 522$ , demonstrating the self-stabilization architecture. The spectrum is normalized to 1 mW, i.e. equivalent to dBm. **c** Locked CEO beat spectrum referenced to the 10 MHz standard (inset: free-running CEO), confirming pre-chip CEO control. RBW: resolution bandwidth. **d** Locked  $\nu_{\text{rep}}^{\text{PDCS}}$  detected at 280 THz (top) and C-band detected  $\nu_{\text{rep}}^{\text{PDCS}}$  (bottom), verifying a single repetition rate across the synchronized PDCS spectrum. **e** Allan deviation of the PDCS comb teeth ( $n = 260$  to 265), showing a  $1/\tau$  slope characteristic of optical frequencies that are synchronized to the microwave reference. Error bars are one standard deviation quantities. Right inset: Schematic of the PDCS acting as a coherent microwave-to-optical link (shaded), with measured downconversion using a fiber OFC. Left inset: Allan deviation of  $\nu_{\text{rep}}^{\text{PDCS}}$  measured in the C-band with clear  $1/\tau$  trend. The deviation at  $\tau < 1$  is due to the EOcomb apparatus. DUT: device under test. **f** Frequency counting accuracy: measured PDCS comb teeth agree with expected values  $\nu_{\text{expected}} = n\nu_{\text{rep}}^{\text{PDCS}} + \nu_{\text{CEO}}^{\text{PDCS}}$ , demonstrating a precise microwave-to-optical link needed for optical frequency synthesis.

$\nu_-$ ). Therefore, when self-aligned,  $\nu_{\text{rep}}$  depends linearly on the pump detunings  $\delta\nu_{\pm}$ , changing sign between positive and negative pump actuation, with slope magnitude  $1/N = 1/(n_+ - n_-) = 1/n_-$  corresponding to the optical frequency division (OFD) factor, as observed experimentally (Fig. 2d). Due to the self-alignment, the repetition rate noise depends only on the frequency noise of the two pumps, as we discuss below, leading to a drastically reduced linewidth compared to the free-running case with three distinct comb components (Fig. 2e).

#### Self-aligned PDCS metrology: microwave to optical link and vice versa

To demonstrate the potential of the self-aligned PDCS OFC, we show its straightforward implementation in metrology applications. As previously described, the two input lasers, separated by an octave, enable definition of a locked CEO frequency that the subsequently generated PDCS must possess. Self-stabilization of the OFC becomes equivalent to locking the two pumps to each other

(with the heterodyne beat provided through nonlinear interferometry via second harmonic generation (SHG)), while another degree of freedom remains available for optical or repetition rate locking. Thus, rather than a dedicated DKS for a specific application, our integrated self-aligned PDCS operates bidirectionally—upstream from microwave to optical frequencies or downstream from optical to microwave frequencies using the same comb—simply by changing only the input laser’s locking point. Though standard for commercial fiber-based frequency combs, such operation has not been readily available in the past using microcombs.

First, we demonstrate self-stabilization of our PDCS, where both  $\nu_{\text{rep}}^{\text{PDCS}}$  and  $\nu_{\text{CEO}}^{\text{PDCS}}$  are locked to a microwave standard, enabling precise knowledge of all optical frequency comb teeth. These teeth could then serve as the reference frequency grid for locking a laser for optical frequency synthesis<sup>29</sup> or as a wavemeter.<sup>42</sup> To showcase the flexibility of self-aligned PDCS generation, enabled by coupling engineering, we use a different microring (with

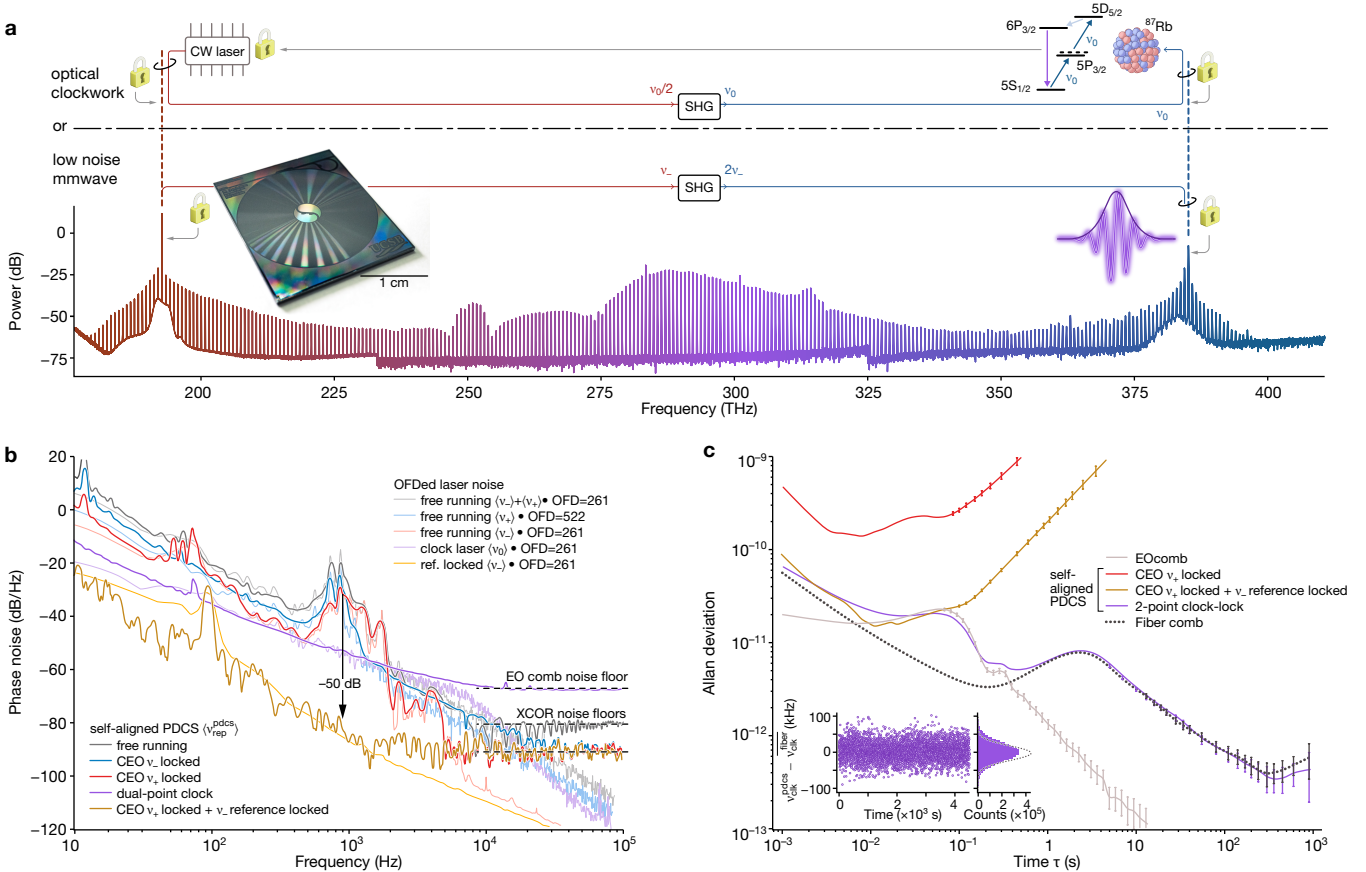


**Fig. 4 – Optical-to-millimeter wave link: low noise millimeter wave generation and optical clockwork operation**—**a** Experimental system for optical-to-millimeter wave link. Using the same self-aligned PDCS as previously, the system can be reconfigured by changing only the input locks. With the two pumps an octave apart, the system seamlessly acts as a low-noise millimeter wave generator when locking the CEO and remaining laser to an integrated silicon nitride reference cavity, or as an optical clockwork when locking the input lasers to the laser-locked rubidium two-photon clock transition. The spectrum is normalized to 1 mW, i.e. equivalent to dBm. **b** PDCS repetition rate phase noise spectral power density  $\langle \nu_{\text{rep}}^{\text{PDCS}} \rangle$  under different input laser configurations: free running (grey), CEO locked with negative pump (blue), CEO locked with positive pump (red), both lasers locked to fundamental and second harmonic of the laser probing the atomic transition (purple), and CEO locked with positive pump while negative pump locks to a reference cavity resonance (yellow). The corresponding laser noise divided by the expected OFD factor in each case appears in matching colors, and is well-aligned with the PDCS repetition rate noise, demonstrating coherent OFD. The phase noise densities are normalized to 1 mW, i.e. equivalent to dBc/Hz. **c** Allan deviation comparing different locking configurations. Error bars are one standard deviation quantities. The free-running negative pump and CEO locked with positive pump configuration exhibits a rapid random frequency walk (red). The reference cavity locked configuration, while showing the best phase noise performance, drifts in frequency over time, leading to poor averaging for  $\tau > 0.1$  s (yellow). The atomic clock locked PDCS demonstrates good long-term averaging (purple), and matches that of a commercial fiber OFC (black dotted) that probes the atomic clock's stability over periods of  $\tau > 1$  s. The discrepancy between the fiber comb and PDCS at  $\tau < 0.1$  s originates from the EOcomb apparatus (grey) used to frequency down-convert the PDCS repetition rate to a detectable frequency. Bottom inset: We count the clock frequency from the PDCS and fiber comb repetition rate in time,  $\nu_{\text{clk}}^{\text{PDCS}}$  and  $\nu_{\text{clk}}^{\text{fiber}}$ , respectively. Both produce identical statistics, highlighted by the centered Gaussian distribution of  $\nu_{\text{clk}}^{\text{PDCS}}$  against the fiber comb average  $\overline{\nu_{\text{clk}}^{\text{fiber}}}$ .

$RW = 860$  nm) from the one used to obtain the results shown in Fig. 2. We set both pump lasers at harmonic comb tooth modes ( $n_+ = 2n_- = 522$ ) of the PDGS, tap a portion of the pre-amplified pump lasers before the chip (Fig. 3a), double the negative pump  $\nu_-$ , and measure the CEO through via a EOcomb from  $\nu_+$  (Fig. 3c inset; see also Methods and Section S.8, and note that the beat between  $\nu_+$  and  $2\nu_-$  is too large for direct photodetection). After generating the self-aligned PDGS, we lock the downconverted  $\nu_{\text{CEO}}^{\text{PDCS}}$  to a 10 MHz rubidium microwave standard (Fig. 3c inset) through feedback onto  $\nu_+$ . At the output, we measure  $\nu_{\text{rep}}^{\text{PDCS}}$  in the 280 THz band with another EOcomb downconverter apparatus

(Section S.8) and lock it to the same 10 MHz reference (Fig. 3d), feeding back onto  $\nu_-$ .

We verify that the self-aligned PDGS is stabilized to the microwave reference by confirming that  $\nu_{\text{rep}}^{\text{PDCS}}$  is consistent across the OFC spectrum and that all comb teeth carry the same relative stability as the reference. First, we measure  $\nu_{\text{rep}}^{\text{PDCS}}$  using a third EOcomb downconverter apparatus, now in the C-band, and confirm the same  $\nu_{\text{rep}}^{\text{PDCS}}$  130 comb teeth away from the lock point (Fig. 3d). The detected  $\nu_{\text{rep}}^{\text{PDCS}}$  synchronizes to the microwave reference for long-term stability (Fig. 3e inset), despite short-term discrepancies that originate from the EOcomb downconversion apparatus, confirming the self-

aligned PDCS has a single repetition rate pinned by the two pump lasers. We measure the long-term stability of the self-aligned PDCS comb teeth from  $n = 260$  to  $n = 265$  using a commercial fiber OFC with CEO locked to the same microwave reference and its  $k^{\text{th}}$  comb tooth locked to the  $n^{\text{th}}$  selected PDCS tooth, enabling coherent frequency division onto the fiber OFC's repetition rate at 125 MHz. All selected PDCS comb teeth exhibit a  $1/\tau$  Allan deviation slope (Fig. 3e), demonstrating the coherent link between the microwave and optical domains, and synchronization to the microwave reference. The modified Allan deviation shows a  $1/\tau^{3/2}$  slope, confirming white phase noise and synchronization. Finally, we count the optical frequency of the comb teeth (Fig. 3f), which exhibit a Gaussian distribution centered around the expected value from the PDCS locked values of  $\nu_{\text{rep}}^{\text{pdc}}$  and  $\nu_{\text{ceo}}^{\text{pdc}}$ .

Next we demonstrate octave-separated optical two-point locking that enables coherent OFD from two locked optical tones onto the repetition rate of the self-aligned PDCS, which, with the same architecture, enables either low-noise millimeter-wave generation or optical clockwork operation (Fig. 4). Unlike narrow-band two-point locking schemes that typically pin two comb teeth separated by  $\approx 60$  teeth through feedback to a single degree of freedom (the single pump),<sup>36,37</sup> our system provides two orthogonal degrees of freedom via the pump lasers, enabling complete stabilization of the repetition rate at the input side. Additionally, the octave separation maximizes the OFD factor to  $n_+ = 522$  by incorporating the CEO into the two-point locking scheme, while simultaneously enabling long-term stabilization through clockwork operation and locking to a stable atomic transition within the same architecture. Hence, we operate with the same self-aligned PDCS as previously in Fig. 3, changing only the input laser lock point (Fig. 4a). In one case, before the chip, the CEO is locked similarly to the previous experiment feedbacking onto one pump laser, while now the other remaining pump laser is locked to an integrated  $\text{Si}_3\text{N}_4$  cavity reference<sup>43</sup> (see Methods). In the other, both pump lasers are locked to a continuous wave laser and its second harmonic SH, the latter is locked to the  $^{87}\text{Rb}$  two-photon clock transition<sup>44</sup> (see Methods) in a vapor cell and detection apparatus similar to ref 45.

We study the phase noise spectral density of the PDCS repetition rate ( $\nu_{\text{rep}}$ ). The PDCS divides down the laser noise ( $\langle \nu_- \rangle$ ,  $\langle \nu_+ \rangle$  or both) onto  $\langle \nu_{\text{rep}} \rangle$  according to the dual-pinning configuration (Fig. 4b). Free running pump lasers lead to  $\langle \nu_{\text{rep}} \rangle = (\langle \nu_- \rangle + \langle \nu_+ \rangle)/n_-$ . By contrast, locking the CEO on the negative pump leads to  $\langle \nu_{\text{rep}} \rangle = \langle \nu_+ \rangle/n_+$ , while locking the CEO on the positive pump leads to  $\langle \nu_{\text{rep}} \rangle = \langle \nu_- \rangle/n_-$ . It is assumed that the CEO locking noise is negligible since it is further optically frequency divided,  $\langle \nu_{\text{ceo}}^{\text{pdc}} \rangle/n_{\pm}$ . Once the CEO is locked by feedback to the positive pump laser  $\nu_+$  and the remaining negative pump laser  $\nu_-$  is locked to a  $\text{Si}_3\text{N}_4$  integrated cavity reference<sup>43</sup> to reduce its noise, the transduced  $\langle \nu_{\text{rep}} \rangle$  exhibits the expected 50 dB reduc-

tion, demonstrating optical frequency division operation of the self-aligned PDCS. Although we use dual-detection of  $\nu_{\text{rep}}^{\text{pdc}}$  in the 280 THz and 190 THz bands for cross-correlation detection (see Section S.7), removing uncorrelated noise from both EOcomb frequency downconverters and reducing noise by more than 25 dB compared to  $\nu_{\text{rep}}$  detection with a single EOcomb downconverter, the lasers' long-term frequency drift prevents extended averaging. As a result, the noise floor exceeds the OFD of the laser noise above 10 kHz, which we expect will be further improved in future work.

We next proceed to demonstrate the use of the same self-aligned PDCS as an optical clockwork, changing only the input laser to be locked to the  $^{87}\text{Rb}$ -SH-stabilized CW laser. We note that the phase noise, which we confirm is transferred from the lasers onto  $\nu_{\text{rep}}^{\text{pdc}}$  via OFD, exceeds that of the reference-locked case (Fig. 4b), which is to be expected given the relatively broad linewidth of the Rb two-photon clock transition in comparison to that of the cavity reference, and the purpose of the atomic reference is to provide the long-term stability, while the purpose of the cavity resonance is to provide short-term stability. To that end, we note that in both the free-running and cavity reference-locked self-aligned PDCS cases, the Allan deviation rises rapidly after short averaging time  $\tau$ , it averages down in the clock-locked case (Fig. 4c). To confirm that the self-aligned PDCS acts as a true clockwork, we locked a fiber comb's CEO and one comb tooth to the clock laser, achieving identical Allan deviation performance except at  $\tau < 1$  s, where the PDCS repetition rate noise is dominated by the EOcomb downconverter. We retrieve the measured clock frequency from both the PDCS ( $\nu_{\text{clk}}^{\text{pdc}}$ ) and fiber comb ( $\nu_{\text{clk}}^{\text{fiber}}$ ) clockworks (see Methods) via repetition rate frequency counting. The PDCS shows a centered Gaussian frequency counting distribution (Fig. 4c inset) offset from  $\nu_{\text{clk}}^{\text{fiber}}$  by about 3 kHz, well within the about 26 kHz standard deviation for seventy-five minutes of statistics. Both the fiber comb and the PDCS exhibit measured clock frequency offsets of  $(-95 \pm 25)$  kHz and  $(-92 \pm 31)$  kHz compared to the accepted value from literature,<sup>30,46–50</sup> respectively, which we attribute to a fixed frequency shift in the experimental apparatus (likely the Rb two-photon frequency reference).

## Discussion

We demonstrate the generation and self-alignment of parametric dissipative cavity solitons from bichromatic pumping of foundry-fabricated silicon nitride microrings. We show that these solitons can synchronize spontaneously with octave-separated pump lasers, forming a single grid of frequency markers from the C-band to the visible, which we leverage to demonstrate the three canonical tasks of optical frequency comb operation. Our self-aligned PDCS microcomb operates in a significantly different manner than standard DKS microcombs that rely on outward cascading from a centered single pump laser, which results in weak edge power, as well as comb

tooth positions and a total span that are not fully predictable *a priori*, all of which complicate CEO detection and the locking that is needed for precision metrology. In contrast, the quasi-harmonic pumping of our system means that the comb span and CEO of the subsequently generated PDCS is set before the chip, enabling robust operation. Moreover, the intrinsic two-point locking that stems from the two input pumps generating and synchronizing the PDCS enables octave-separated orthogonal control of all the integrated OFC's degrees of freedom. Thus, such novel approach provides a versatile and bi-directional reconfiguration so that the same PDCS can be used as a coherent bridge between the microwave and optical domains. We demonstrate the benefit of this versatility by performing three key tasks for integrated OFC systems: self-referencing to establish a stable frequency grid that can serve as a backbone for optical frequency synthesizers or wavemeters, two-point optical locking (including the CEO) for low-noise millimeter wave generation, and optical clockwork for transferring the relative stability of the  $^{87}\text{Rb}$  atomic clock transition to the PDCS repetition rate.

Moving forward, our self-aligned PDCS enables several integration capabilities, many of which stem from the stabilized, octave-separated pumps that remain available for further use. For example, the system is highly suitable for integrated second harmonic generation of the negative pump for high signal-to-noise ratio CEO detection, without any requirement for extremely high normalized conversion efficiency, since the available pump powers are in the 10 mW range. This is particularly compelling for monolithic integration with photogalvanic-induced SHG in silicon nitride microresonators,<sup>51,52</sup> which would enable a complete OFC clockwork in a single fabrication process. In addition, there is significant potential to use nonlinear processes that involve one or both pump lasers, whose frequencies are precisely known from PDCS self stabilization, to generate stable continuous wave reference tones outside of the PDCS spectral window. Processes such as second and third harmonic generation and sum frequency generation can enable interfacing with atomic systems used in quantum sensing<sup>53,54</sup> and higher-performance optical clocks.<sup>55–58</sup> Finally, while the PDCS center frequency operates in the anomalous dispersion regime, both pumps reside in the normal dispersion regime. As a result, we expect that with appropriate dispersion engineering and pump frequency selection, self-aligned PDCSs can realize bandwidths exceeding those thus far demonstrated with standard DKSs, which has been limited to about an octave. We anticipate that the span and wavelength access ( $> 350$  THz and down to 532 nm, respectively) of ultra-broadband optical parametric oscillators recently demonstrated in the same silicon nitride platform<sup>59</sup> can be utilized for PDCSs.

In conclusion, our self-aligned PDCS presents a foundry-compatible paradigm shift in integrated frequency metrology by inverting the architectural approach that has confined on-chip frequency combs to laboratory

settings. Rather than miniaturizing existing designs, this octave-bounded generation scheme is a critical step in fulfilling the long-standing promise of field-deployable precision optical frequency combs for navigation, quantum technologies, and fundamental physics measurements.

---

[1] S. A. Diddams, K. Vahala, and T. Udem, Optical frequency combs: Coherently uniting the electromagnetic spectrum, *Science* **369**, eaay3676 (2020).

[2] T. J. Kippenberg, A. L. Gaeta, M. Lipson, and M. L. Gorodetsky, Dissipative Kerr solitons in optical microresonators, *Science* **361**, eaan8083 (2018).

[3] Q. Li, T. C. Briles, D. A. Westly, T. E. Drake, J. R. Stone, B. R. Ilic, S. A. Diddams, S. B. Papp, and K. Srinivasan, Stably accessing octave-spanning microresonator frequency combs in the soliton regime, *Optica* **4**, 193 (2017).

[4] T. E. Drake, J. R. Stone, T. C. Briles, and S. B. Papp, Thermal decoherence and laser cooling of Kerr microresonator solitons, *Nature Photonics* **14**, 480 (2020).

[5] N. Englebert, F. De Lucia, P. Parra-Rivas, C. M. Arabí, P.-J. Sazio, S.-P. Gorza, and F. Leo, Parametrically driven Kerr cavity solitons, *Nature Photonics* **15**, 857 (2021).

[6] G. Moille, M. Leonhardt, D. Paligora, N. Englebert, F. Leo, J. Fatome, K. Srinivasan, and M. Erkintalo, Parametrically driven pure-Kerr temporal solitons in a chip-integrated microcavity, *Nature Photonics* **18**, 617 (2024).

[7] M. A. Lombardi, Microsecond accuracy at multiple sites: Is it possible without GPS?, *IEEE Instrumentation & Measurement Magazine* **15**, 14 (2012).

[8] R. Finkelstein, R. B.-S. Tsai, X. Sun, P. Scholl, S. Direkci, T. Gefen, J. Choi, A. L. Shaw, and M. Endres, Universal quantum operations and ancilla-based read-out for tweezer clocks, *Nature* **634**, 321 (2024).

[9] J. Ye and P. Zoller, Essay: Quantum Sensing with Atomic, Molecular, and Optical Platforms for Fundamental Physics, *Physical Review Letters* **132**, 190001 (2024).

[10] C. Lisdat, G. Grosche, N. Quintin, C. Shi, S. M. F. Raupach, C. Grebing, D. Nicolodi, F. Stefani, A. Al-Masoudi, S. Dörscher, S. Häfner, J.-L. Robyr, N. Chiodo, S. Bilicki, E. Bookjans, A. Koczwara, S. Koke, A. Kuhl, F. Wiotte, F. Meynadier, E. Camisard, M. Abgrall, M. Lours, T. Legero, H. Schnatz, U. Sterr, H. Denker, C. Chardonnet, Y. Le Coq, G. Santarelli, A. Amy-Klein, R. Le Targat, J. Lodewyck, O. Lopez, and P.-E. Pottie, A clock network for geodesy and fundamental science, *Nature Communications* **7**, 12443 (2016).

[11] A. Derevianko, K. Gibble, L. Hollberg, N. R. Newbury, C. Oates, M. S. Safronova, L. C. Sinclair, and N. Yu, Fundamental physics with a state-of-the-art optical clock in space, *Quantum Science and Technology* **7**, 044002 (2022).

[12] N. Dimarcq, M. Gertsvolf, G. Miletí, S. Bize, C. W. Oates, E. Peik, D. Calonico, T. Ido, P. Tavella, F. Meynadier, G. Petit, G. Panfilo, J. Bartholomew, P. Defraigne, E. A. Donley, P. O. Hedekvist, I. Sesia, M. Wouters, P. Dubé, F. Fang, F. Levi, J. Lodewyck, H. S. Margolis, D. Newell, S. Slyusarev, S. Weyers, J.-P. Uzan, M. Yasuda, D.-H. Yu, C. Rieck, H. Schnatz, Y. Hanado, M. Fujieda, P.-E. Pottie, J. Hanssen, A. Malimon, and N. Ashby, Roadmap towards the redefinition of the second, *Metrologia* **61**, 012001 (2024).

[13] F. Riehle, Towards a redefinition of the second based on optical atomic clocks, *Comptes Rendus. Physique* **16**, 506 (2015).

[14] A. J. Metcalf, T. Anderson, C. F. Bender, S. Blakeslee, W. Brand, D. R. Carlson, W. D. Cochran, S. A. Diddams, M. Endl, C. Fredrick, S. Halverson, D. D. Hickstein, F. Hearty, J. Jennings, S. Kanodia, K. F. Kaplan, E. Levi, E. Lubar, S. Mahadevan, A. Monson, J. P. Ninan, C. Nitroy, S. Osterman, S. B. Papp, F. Quinlan, L. Ramsey, P. Robertson, A. Roy, C. Schwab, S. Sigurdsson, K. Srinivasan, G. Stefansson, D. A. Sterner, R. Terrien, A. Wolszczan, J. T. Wright, and G. Ycas, Stellar spectroscopy in the near-infrared with a laser frequency comb, *Optica* **6**, 233 (2019).

[15] R. Holzwarth, Th. Udem, T. W. Hänsch, J. C. Knight, W. J. Wadsworth, and P. St. J. Russell, Optical Frequency Synthesizer for Precision Spectroscopy, *Physical Review Letters* **85**, 2264 (2000).

[16] T. M. Fortier, M. S. Kirchner, F. Quinlan, J. Taylor, J. C. Bergquist, T. Rosenband, N. Lemke, A. Ludlow, Y. Jiang, C. W. Oates, and S. A. Diddams, Generation of ultrastable microwaves via optical frequency division, *Nature Photonics* **5**, 425 (2011).

[17] A. W. Bruch, X. Liu, Z. Gong, J. B. Surya, M. Li, C.-L. Zou, and H. X. Tang, Pockels soliton microcomb, *Nature Photonics* **15**, 21 (2021).

[18] T.-H. Wu, L. Ledezma, C. Fredrick, P. Sekhar, R. Sekine, Q. Guo, R. M. Briggs, A. Marandi, and S. A. Diddams, Visible-to-ultraviolet frequency comb generation in lithium niobate nanophotonic waveguides, *Nature Photonics* **18**, 218 (2024).

[19] P. Del'Haye, A. Coillet, T. Fortier, K. Beha, D. C. Cole, K. Y. Yang, H. Lee, K. J. Vahala, S. B. Papp, and S. A. Diddams, Phase-coherent microwave-to-optical link with a self-referenced microcomb, *Nature Photonics* **10**, 516 (2016).

[20] D. D. Hickstein, H. Jung, D. R. Carlson, A. Lind, I. Coddington, K. Srinivasan, G. G. Ycas, D. C. Cole, A. Kowlgy, C. Fredrick, S. Droste, E. S. Lamb, N. R. Newbury, H. X. Tang, S. A. Diddams, and S. B. Papp, Ultrabroadband Supercontinuum Generation and Frequency-Comb Stabilization Using On-Chip Waveguides with Both Cubic and Quadratic Nonlinearities, *Physical Review Applied* **8**, 014025 (2017).

[21] H. Telle, G. Steinmeyer, A. Dunlop, J. Stenger, D. Suter, and U. Keller, Carrier-envelope offset phase control: A novel concept for absolute optical frequency measurement and ultrashort pulse generation, *Applied Physics B* **69**, 327 (1999).

[22] D. J. Jones, S. A. Diddams, J. K. Ranka, A. Stentz, R. S. Windeler, J. L. Hall, and S. T. Cundiff, Carrier-Envelope Phase Control of Femtosecond Mode-Locked Lasers and Direct Optical Frequency Synthesis, *Science* **288**, 635 (2000).

[23] J. Liu, G. Huang, R. N. Wang, J. He, A. S. Raja, T. Liu, N. J. Engelsen, and T. J. Kippenberg, High-yield, wafer-scale fabrication of ultralow-loss, dispersion-engineered silicon nitride photonic circuits, *Nature Communications* **12**, 2236 (2021).

[24] S.-C. Ou, A. O. Antohe, L. G. Carpenter, G. Moille, and K. Srinivasan, 300 mm wafer-scale SiN platform for broadband soliton microcombs compatible with alkali atomic references, *Optics Letters* **50**, 5578 (2025).

[25] B. Stern, X. Ji, Y. Okawachi, A. L. Gaeta, and M. Lipson,

Battery-operated integrated frequency comb generator, *Nature* **562**, 401 (2018).

[26] Y. Sun, J. Wu, M. Tan, X. Xu, Y. Li, R. Morandotti, A. Mitchell, and D. J. Moss, Applications of optical microcombs, *Advances in Optics and Photonics* **15**, 86 (2023).

[27] E. Lucas, H. Guo, J. D. Jost, M. Karpov, and T. J. Kippenberg, Detuning-dependent properties and dispersion-induced instabilities of temporal dissipative Kerr solitons in optical microresonators, *Physical Review A* **95**, 043822 (2017).

[28] V. Brasch, E. Lucas, J. D. Jost, M. Geiselmann, and T. J. Kippenberg, Self-referenced photonic chip soliton Kerr frequency comb, *Light: Science & Applications* **6**, e16202 (2017).

[29] D. T. Spencer, T. Drake, T. C. Briles, J. Stone, L. C. Sinclair, C. Fredrick, Q. Li, D. Westly, B. R. Ilic, A. Bluestone, N. Volet, T. Komljenovic, L. Chang, S. H. Lee, D. Y. Oh, M.-G. Suh, K. Y. Yang, M. H. P. Pfeiffer, T. J. Kippenberg, E. Norberg, L. Theogarajan, K. Vahala, N. R. Newbury, K. Srinivasan, J. E. Bowers, S. A. Diddams, and S. B. Papp, An optical-frequency synthesizer using integrated photonics, *Nature* **557**, 81 (2018).

[30] Z. L. Newman, V. Maurice, T. Drake, J. R. Stone, T. C. Briles, D. T. Spencer, C. Fredrick, Q. Li, D. Westly, B. R. Ilic, B. Shen, M.-G. Suh, K. Y. Yang, C. Johnson, D. M. S. Johnson, L. Hollberg, K. J. Vahala, K. Srinivasan, S. A. Diddams, J. Kitching, S. B. Papp, and M. T. Hummon, Architecture for the photonic integration of an optical atomic clock, *Optica* **6**, 680 (2019).

[31] K. Wu, N. P. O’Malley, S. Fatema, C. Wang, M. Girardi, M. S. Alshaykh, Z. Ye, D. E. Leaird, M. Qi, V. Torres-Company, and A. M. Weiner, Vernier microcombs for high-frequency carrier envelope offset and repetition rate detection, *Optica* **10**, 626 (2023).

[32] G. Moille, P. Shandilya, J. Stone, C. Menyuk, and K. Srinivasan, All-optical noise quenching of an integrated frequency comb, *Optica* **12**, 1020 (2025).

[33] K. Wu, N. P. O’Malley, S. Fatema, C. Wang, M. Girardi, M. S. Alshaykh, Z. Ye, D. E. Leaird, M. Qi, V. Torres-Company, and A. M. Weiner, Vernier microcombs for integrated optical atomic clocks, *Nature Photonics* **19**, 400 (2025).

[34] G. Moille, J. Stone, M. Chojnacky, R. Shrestha, U. A. Javid, C. Menyuk, and K. Srinivasan, Kerr-induced synchronization of a cavity soliton to an optical reference, *Nature* **624**, 267 (2023).

[35] C. R. Menyuk, P. Shandilya, L. Courtright, G. Moille, and K. Srinivasan, Multi-color solitons and frequency combs in microresonators, *Optics Express* **33**, 21824 (2025).

[36] S. B. Papp, K. Beha, P. Del’Haye, F. Quinlan, H. Lee, K. J. Vahala, and S. A. Diddams, Microresonator frequency comb optical clock, *Optica* **1**, 10 (2014).

[37] I. Kudelin, W. Groman, Q.-X. Ji, J. Guo, M. L. Kelleher, D. Lee, T. Nakamura, C. A. McLemore, P. Shirmohammadi, S. Hanifi, H. Cheng, N. Jin, L. Wu, S. Halladay, Y. Luo, Z. Dai, W. Jin, J. Bai, Y. Liu, W. Zhang, C. Xiang, L. Chang, V. Iltchenko, O. Miller, A. Matsko, S. M. Bowers, P. T. Rakich, J. C. Campbell, J. E. Bowers, K. J. Vahala, F. Quinlan, and S. A. Diddams, Photonic chip-based low-noise microwave oscillator, *Nature* **627**, 534 (2024).

[38] A. Diakonov, K. Khrizman, and L. Stern, *Hybrid-Locked Kerr Microcombs for Flexible On-Chip Optical Clock Division* (2025), arXiv:2508.07258 [physics].

[39] G. Moille, Q. Li, T. C. Briles, S.-P. Yu, T. Drake, X. Lu, A. Rao, D. Westly, S. B. Papp, and K. Srinivasan, Broadband resonator-waveguide coupling for efficient extraction of octave-spanning microcombs, *Optics Letters* **44**, 4737 (2019).

[40] H. Zhou, Y. Geng, W. Cui, S.-W. Huang, Q. Zhou, K. Qiu, and C. Wei Wong, Soliton bursts and deterministic dissipative Kerr soliton generation in auxiliary-assisted microcavities, *Light: Science & Applications* **8**, 50 (2019).

[41] S. Zhang, J. M. Silver, L. Del Bino, F. Copie, M. T. M. Woodley, G. N. Ghalanos, A. Ø. Svela, N. Moroney, and P. Del’Haye, Sub-milliwatt-level microresonator solitons with extended access range using an auxiliary laser, *Optica* **6**, 206 (2019).

[42] R. Niu, M. Li, S. Wan, Y. R. Sun, S.-M. Hu, C.-L. Zou, G.-C. Guo, and C.-H. Dong, kHz-precision wavemeter based on reconfigurable microsoliton, *Nature Communications* **14**, 169 (2023).

[43] K. Liu, N. Chauhan, J. Wang, A. Isichenko, G. M. Brodnik, P. A. Morton, R. O. Behunin, S. B. Papp, and D. J. Blumenthal, 36 Hz integral linewidth laser based on a photonic integrated 4.0 m coil resonator, *Optica* **9**, 770 (2022).

[44] K. W. Martin, G. Phelps, N. D. Lemke, M. S. Bigelow, B. Stuhl, M. Wojcik, M. Holt, I. Coddington, M. W. Bishop, and J. H. Burke, Compact Optical Atomic Clock Based on a Two-Photon Transition in Rubidium, *Physical Review Applied* **9**, 014019 (2018).

[45] R. Beard, K. W. Martin, J. D. Elgin, B. L. Kasch, and S. P. Krzyzewski, Two-photon rubidium clock detecting 776 nm fluorescence, *Optics Express* **32**, 7417 (2024).

[46] F. Nez, F. Biraben, R. Felder, and Y. Millerioux, Optical frequency determination of the hyperfine components of the 5S12-5D32 two-photon transitions in rubidium, *Optics Communications* **102**, 432 (1993).

[47] L. Hilico, R. Felder, D. Touahri, O. Acef, A. Clairon, and F. Biraben, Metrological features of the rubidium two-photon standards of the BNM-LPTF and Kastler Brossel Laboratories, *The European Physical Journal Applied Physics* **4**, 219 (1998).

[48] J. E. Bernard, A. A. Madej, K. J. Siemsen, L. Marmet, C. Latrasse, D. Touahri, M. Poulin, M. Allard, and M. Têtu, Absolute frequency measurement of a laser at 1556 nm locked to the 5S1/2-5D5/2 two-photon transition in 87Rb, *Optics Communications* **173**, 357 (2000).

[49] C. S. Edwards, G. P. Barwood, H. S. Margolis, P. Gill, and W. R. C. Rowley, Development and absolute frequency measurement of a pair of 778 nm two-photon rubidium standards, *Metrologia* **42**, 464 (2005).

[50] S. Y. Zhang, J. T. Wu, Y. L. Zhang, J. X. Leng, W. P. Yang, Z. G. Zhang, and J. Y. Zhao, Direct frequency comb optical frequency standard based on two-photon transitions of thermal atoms, *Scientific Reports* **5**, 15114 (2015).

[51] X. Lu, G. Moille, A. Rao, D. A. Westly, and K. Srinivasan, Efficient photoinduced second-harmonic generation in silicon nitride photonics, *Nature Photonics* **15**, 131 (2021).

[52] M. Clementi, L. Zatti, J. Zhou, M. Liscidini, and C.-S. Brès, Ultrabroadband milliwatt-level resonant frequency doubling on a chip, *Nature Communications* **16**, 6164

(2025).

[53] M. Saffman, T. G. Walker, and K. Mølmer, Quantum information with Rydberg atoms, *Reviews of Modern Physics* **82**, 2313 (2010).

[54] C. Pak, M. J. Schlitters, and S. D. Bergeson, Improved ionization potential of calcium using frequency-comb-based Rydberg spectroscopy, *Physical Review A* **106**, 062818 (2022).

[55] A. D. Ludlow, M. M. Boyd, J. Ye, E. Peik, and P. O. Schmidt, Optical atomic clocks, *Reviews of Modern Physics* **87**, 637 (2015).

[56] T. L. Nicholson, S. L. Campbell, R. B. Hutson, G. E. Marti, B. J. Bloom, R. L. McNally, W. Zhang, M. D. Barrett, M. S. Safronova, G. F. Strouse, W. L. Tew, and J. Ye, Systematic evaluation of an atomic clock at  $2 \times 10^{-18}$  total uncertainty, *Nature Communications* **6**, 6896 (2015).

[57] I. Ushijima, M. Takamoto, M. Das, T. Ohkubo, and H. Katori, Cryogenic optical lattice clocks, *Nature Photonics* **9**, 185 (2015).

[58] T. Rosenband, D. B. Hume, P. O. Schmidt, C. W. Chou, A. Brusch, L. Lorini, W. H. Oskay, R. E. Drullinger, T. M. Fortier, J. E. Stalnaker, S. A. Diddams, W. C. Swann, N. R. Newbury, W. M. Itano, D. J. Wineland, and J. C. Bergquist, Frequency Ratio of Al+ and Hg+ Single-Ion Optical Clocks; Metrology at the 17th Decimal Place, *Science* **319**, 1808 (2008).

[59] Y. Sun, J. Stone, X. Lu, F. Zhou, J. Song, Z. Shi, and K. Srinivasan, Advancing on-chip Kerr optical parametric oscillation towards coherent applications covering the green gap, *Light: Science & Applications* **13**, 201 (2024).

[60] Certain commercial equipment is identified to foster understanding. Such identification does not imply recommendation or endorsement by the National Institute of Standards and Technology or the U.S. Government, nor does it imply that the materials or equipment identified are necessarily the best available for the purpose.

[61] H. Taheri, A. B. Matsko, and L. Maleki, Optical lattice trap for Kerr solitons, *The European Physical Journal D* **71**, 153 (2017).

[62] G. Moille, Z. Li, S. Shamailov, M. Leonhardt, D. Paligora, N. Englebert, F. Leo, J. Fatome, K. Srinivasan, and M. Erkintalo, Existence, stability, and characteristics of pure-Kerr parametrically driven cavity solitons, *SPIE Photonics West Laser Resonators, Microresonators, and Beam Control XXVII*, PC1334908 (2025).

[63] C. R. Menyuk and S. Wang, Spectral methods for determining the stability and noise performance of passively modelocked lasers, *Nanophotonics* **5**, 332 (2016).

[64] Z. Qi, S. Wang, J. Caramillo-Villegas, M. Qi, A. M. Weiner, G. D'Aguanno, T. F. Carruthers, and C. R. Menyuk, Dissipate cnoidal waves (turing rolls) and the soliton limit in microresonators, *Optica* **6**, 1220 (2019).

[65] J. M. Lukens, K. V. Mylswamy, A. Miloshevsky, and H.-H. Lu, *Beyond critical coupling: Optimal design considerations for spontaneous four-wave mixing in microring resonators* (2025), arXiv:2511.08563 [quant-ph].

[66] N. S. Tatarinova, A. E. Shitikov, G. V. Grechko, A. K. Vorobyev, A. V. Masalov, I. A. Bilenko, D. A. Chernoshentsev, and V. E. Lobanov, Optimization of the threshold for degenerate optical parametric oscillations in a bichromatically pumped microresonator, *Physical Review Applied* **24**, 024010 (2025).

[67] G. Moille, D. Westly, R. Shrestha, K. T. Hoang, and K. Srinivasan, Broadband Visible Wavelength Micro-comb Generation In Silicon Nitride Microrings Through Air-Clad Dispersion Engineering, *Laser & Photonics Reviews* , 2401746 (2025)

## Methods

### Device design and fabrication

The devices were fabricated at the commercial silicon nitride foundry Ligentec,<sup>60</sup> where a 100 mm (4 in) wafer is patterned with a repeated 22 mm  $\times$  22 mm reticle containing the 1.8 mm  $\times$  5.4 mm chip with the microring designs of interest. The photonic devices are created through a subtractive process, where the  $\text{Si}_3\text{N}_4$  atop a  $\text{SiO}_2$  layer is removed to create the design, and then encapsulated in a top  $\text{SiO}_2$  layer. A bus waveguide of  $W_{\text{wg}} = 500$  nm width, tapered to 200 nm at the facet for edge coupling to lensed fibers, is wrapped in a pulley configuration around the microring with a gap of  $G = 400$  nm between the bus and ring. We set the pulley coupling length to  $L_c = 17$   $\mu\text{m}$  for phase-mismatch engineering to optimize the coupling chromatic dispersion: largely overcoupled at the negative pump  $\nu_-$  and near-critically coupled at the PDCS center frequency  $(\nu_- + \nu_+)/2$  and positive pump  $\nu_+$  (see Fig. S.5(b) and Section S.2). The microring geometry, namely the ring width  $RW$  and  $\text{Si}_3\text{N}_4$  thickness  $H = 650$  nm, is chosen for optimal dispersion conditions where the optical parametric oscillation condition and phase-matching with the DKS occur simultaneously at the octave-apart pump frequencies  $\nu_{\pm}$ . The in-plane parameters, such as  $G$  and  $RW$ , are varied throughout the chip to compensate for fabrication imperfections and provide some lithographic tuning of the PDCS properties.

### PDCS generation protocol

To generate the PDCS, the two pump lasers  $\nu_-$  and  $\nu_+$  are set to the transverse electric (TE) polarization upon injection on-chip to pump the fundamental mode of the microring resonator ( $\text{TE}_0$ ). First, the positive pump  $\nu_+$  is set on resonance; given its near-visible wavelength, it can be directly observed through residual scattering captured by the optical vision apparatus, in addition to transmission spectroscopy. The negative pump  $\nu_-$  thus remains on the blue-detuned side of its resonance. Working with  $\nu_+$  first and parking it offers the main advantage that, since it operates at a shorter wavelength, the residual absorption and resulting heat generated by this laser exceed that of  $\nu_-$  (which is in the C-band). This choice prevents complex nonlinear behavior of the pumps' frequency detunings relative to their resonances, and is similar to the auxiliary laser approach used for thermo-optic stabilization in standard DKS generation.<sup>41</sup> The negative pump is then set close to its resonance, with its piezoelectric element sweeping slowly (20 Hz) across a span of  $\approx 40$  GHz. A fiber wavelength demultiplexer enables probing of the PDCS power without interference from the pump powers (as seen in the Fig. 1b inset).

Overcoupling of the  $\nu_-$  resonance offers two main advantages for PDCS generation: it reduces the thermal impact of the  $\nu_-$  laser (relative to the fixed  $\nu_+$  laser) and enables very large frequency tuning while remaining on resonance. Therefore, any frequency discrepancy in the OPO condition for PDCS generation and/or fre-

quency tuning necessary for self-alignment can be compensated while maintaining  $\nu_-$  on resonance. This makes PDCS generation extremely robust, as it is simply obtained by adiabatic (*i.e.*, manual tuning of the laser actuator) frequency tuning of  $\nu_-$ , and once accessed, the PDCS remains stable over time (over a working day in the self-aligned regime), without active feedback to the lensed fibers or pump lasers. The Section S.4 shows that the PDCS, outside of its self-alignment window, can be maintained for  $> 2$  GHz frequency detuning of  $\nu_-$ .

### Nonlinear dynamics data acquisition

Once the PDCS is generated through the protocol described above, we characterize the self-synchronization presented in Fig. 1 and Section S.5. The resonator operates in a small dispersive regime within the bandwidth of interest between  $\nu_-$  and  $\nu_+$ , where the nonlinearity suffices to lock the group velocity between the soliton and any pumped component.<sup>6</sup> Outside of synchronization, the only degree of freedom within the resonator is the phase velocity mismatch, which leads to frequency interleaving of the PDCS and the pumped components. This offset  $\Delta\nu_{\text{ceo}}$  is equal in magnitude but opposite in sign between the PDCS and the  $\nu_+$  component and the PDCS and  $\nu_-$  component. Once synchronized, all phases lock, creating a single frequency grid with a single CEO. To determine synchronization, we measure  $\Delta\nu_{\text{ceo}}$  and its vanishing when self-alignment occurs. The pumped component and PDCS spectra overlap throughout the spectrum, which becomes apparent when working in a soliton crystal state, where the different components can be segregated based on their interleaving (Fig. S.6). We detect  $\Delta\nu_{\text{ceo}}$  by filtering the complete spectrum around 300 THz (*i.e.* 980 nm) using a wavelength demultiplexer (WDM) and a 6 GHz photodiode. We reconstruct the spectrogram by measuring the temporal signal of  $\Delta\nu_{\text{ceo}}$  while sweeping  $\nu_-$ . Using the `scipy.signal` python package, we reconstruct the temporal spectrogram. We calibrate the negative pump detuning  $\delta\nu_-$  by similarly creating a spectrogram of the heterodyne between  $\nu_-$  and a 125 MHz fiber optical frequency comb. A similar procedure is used for the positive pump detuning  $\nu_+$ . As in standard KIS, the non-zero phase locking window means that the soliton self-adapts to maintain the synchronization condition while the repetition rate can undergo a frequency shift. Therefore,  $\nu_{\text{rep}}^{\text{pdc}}$  is also disciplined in the self-aligned PDCS case. We measure  $\nu_{\text{rep}}^{\text{pdc}}$  using an electro-optic comb (EOcomb) downconversion scheme similar to Ref.<sup>32</sup> This consists of two cascaded phase modulators that are overdriven by a microwave synthesizer at  $\nu_{\text{rf}}^{\text{rep}}$  to create many sidebands. By modulating two adjacent PDCS comb teeth around 280 THz so that each generates sidebands that span at least  $\nu_{\text{rep}}^{\text{pdc}} \approx 735$  GHz, the  $m^{\text{th}}$  sideband from the two PDCS comb teeth will be offset from each other by a frequency  $\nu_{\text{IF}}^{\text{rep}}$  within the photodiode detection bandwidth (50 MHz). The EO comb thus acts as a local oscillator, enabling frequency down-conversion of  $\nu_{\text{rep}}^{\text{pdc}}$  into a de-

etectable frequency  $\pm\nu_{\text{IF}}^{\text{rep}} = \nu_{\text{rep}}^{\text{pdcs}} - m\nu_{\text{rf}}^{\text{rep}}$ . The sign is determined by whether the modulated PDCS sidebands cross before the overlap; in our case, they are always set to avoid a crossing (*i.e.*, positive sign). Because of the linear relationship between the repetition rate  $\nu_{\text{rep}}^{\text{pdcs}}$  and its frequency down-converted signal  $\nu_{\text{IF}}^{\text{rep}}$ , we can directly map  $\partial\nu_{\text{IF}}^{\text{rep}}/\partial\nu_{\pm} = \partial\nu_{\text{rep}}^{\text{pdcs}}/\partial\nu_{\pm}$  as we keep the EO comb fixed. Similarly to  $\Delta\nu_{\text{ceo}}$ , we record the temporal signal of  $\nu_{\text{IF}}^{\text{rep}}$  while sweeping  $\delta\nu_-$  and reconstruct the spectrogram.

### Microwave-to-optical link experiment

Self-stabilization of the PDCS is achieved by phase-locking the repetition rate  $\nu_{\text{rep}}^{\text{pdcs}}$  and the carrier-envelope offset (CEO) frequency  $\nu_{\text{ceo}}^{\text{pdcs}}$ . To set  $\nu_{\text{ceo}}^{\text{pdcs}}$ , we double the negative pump  $\nu_-$  through second-harmonic generation (SHG) before the PDCS chip and beat it against the positive pump  $\nu_+$ . Because the PDCS self-aligns through self-KIS to the two pump lasers, both pumps are comb teeth; performing this measurement on the input side is thus analogous to standard  $f - 2f$  nonlinear interferometry for CEO retrieval, but is done before the comb is generated, is intrinsically low-noise (*i.e.*, only the two lasers contribute, with no impact from the microring cavity or PDCS intrinsic noise), and exhibits a very large signal-to-noise ratio. For setting  $\nu_{\text{ceo}}^{\text{pdcs}}$ , the two lasers are tapped from the input using respective 10 % couplers (without amplification), and we obtain  $P_{2\nu_-} \approx 10 \mu\text{W}$  and  $P_{\nu_+} \approx 1 \text{ mW}$ . Since  $\nu_{\text{ceo}}^{\text{pdcs}}$  is large, its detection is performed using an electro-optic comb apparatus consisting of one phase modulator acting on the positive pump laser to frequency-downconvert  $\nu_{\text{ceo}}^{\text{pdcs}}$  to a 10 MHz beat note such that  $\nu_{\text{IF}}^{\text{ceo}} = \nu_{\text{ceo}}^{\text{pdcs}} - p\nu_{\text{rf}}^{\text{ceo}}$  ( $p$  is the number of electro-optic sidebands). We phase-lock  $\nu_{\text{IF}}^{\text{ceo}}$  to a Rb 10 MHz microwave reference, which serves as the input reference for all microwave synthesizers throughout the setup, by feedback to the positive pump laser. We measure the frequency-downconverted repetition rate  $\nu_{\text{IF}}^{\text{rep}}$  in the 280 THz spectral band and lock it to the same 10 MHz reference. From both locks, we determine the expected PDCS comb tooth frequencies such that  $\nu_{\text{expected}}(n) = n\nu_{\text{rep}}^{\text{pdcs}} + \nu_{\text{ceo}}^{\text{pdcs}} = n(m\nu_{\text{IF}}^{\text{rep}} + \nu_{\text{rf}}^{\text{rep}}) + \nu_{\text{IF}}^{\text{ceo}} + p\nu_{\text{rf}}^{\text{ceo}}$ .

We measure an individual PDCS comb tooth frequency and stability using a commercial fiber optical frequency comb with repetition rate  $\nu_{\text{rep}}^{\text{fiber}} \approx 125 \text{ MHz}$ . We leverage the coherent two-way bridge between optical and microwave frequencies to count the PDCS comb teeth. Although one could self-reference the fiber comb by locking its CEO and repetition rate, and then heterodyne one fiber comb tooth against one PDCS tooth, the noise multiplication from such an upstream scheme produces excessive noise in the fiber comb teeth given the modest noise performance of our Rb 10 MHz microwave reference, rendering such frequency counting impossible. Instead, we leverage optical frequency division. In this scheme, we lock the fiber comb CEO  $\nu_{\text{ceo}}^{\text{fiber}}$  to the 10 MHz microwave reference and phase-lock one fiber comb tooth to one PDCS tooth at a given frequency offset  $\delta_{\text{lock}}$  ref-

erenced to the same Rb reference. By directly detecting and counting  $\nu_{\text{rep}}^{\text{fiber}}$ , we retrieve the PDCS comb tooth frequency and stability with  $\nu_{\text{meas}}(n) = k\nu_{\text{rep}}^{\text{fiber}} + \nu_{\text{ceo}}^{\text{fiber}} \pm \delta_{\text{lock}}$ , where  $k$  is the fiber comb tooth order that locks to the PDCS, and the sign before the lock offset depends on the mode number. The measurements presented in Fig. 3 are performed deliberately with different  $\nu_{\text{ceo}}^{\text{pdcs}}$  and  $\nu_{\text{rep}}^{\text{pdcs}}$  conditions by actuating the pump laser, demonstrating that the self-aligned PDCS comb teeth are predictable regardless of the self-stabilization operating point.

### Optical-to-microwave link experiment

We use the same self-aligned PDCS as in the microwave-to-optics experiment, but modify the locks of the input lasers. In one scenario to generate low-noise millimeter waves, we set the CEO of the PDCS similarly by doubling the input negative laser and beating it against the input positive laser, followed by phase-locking the EO frequency down-converted tone to a 10 MHz reference with feedback on either laser depending on the scheme. The remaining laser can either remain free or be locked to a reference cavity. When the CEO is locked through  $\nu_+$ , we use an integrated 10 m coiled-spiral microcavity reference made of  $\text{Si}_3\text{N}_4$  and embedded in  $\text{SiO}_2$ , similar to that used in Ref.,<sup>43</sup> and packaged with direct fiber pigtail access. Using a Pound-Drever-Hall technique, where the input laser  $\nu_-$  is phase-modulated at 25 MHz, the laser locks to the dip of the high-Q resonance of the integrated cavity reference. For noise measurement, the repetition rate  $\nu_{\text{rep}}^{\text{pdcs}}$  is detected in the same fashion as before, namely using EO combs as local oscillators to frequency down-convert the repetition rate into a detected window. However, as with every local oscillator down-conversion scheme, the noise of the EO comb imprints on the detected beat note such that  $\langle\nu_{\text{IF}}^{\text{rep}}\rangle = \langle\nu_{\text{rep}}^{\text{pdcs}}\rangle + N\langle\nu_{\text{rf}}^{\text{rep}}\rangle$ . To bypass the noise floor from the EO comb detection, we detect  $\nu_{\text{rep}}^{\text{pdcs}}$  simultaneously in the 280 THz and C-band spectral windows with two independent EO combs and microwave synthesizers. The two down-converted beats enable a cross-correlation (XCOR) measurement, removing the uncorrelated noise from each EO comb and decreasing the noise floor by approximately 25 dB compared to single EO comb  $\nu_{\text{rep}}^{\text{pdcs}}$  detection. This noise floor can be further reduced with larger XCOR averaging, which in our setup is currently limited by  $\nu_{\text{rep}}^{\text{pdcs}}$  frequency drift from the reference cavity frequency drift, as seen in the Allan deviation characterization in Fig. 4c.

For the clockwork measurement, the clock laser is phase-modulated and stabilized using fluorescence detection from the  $^{87}\text{Rb}$  vapor cell, analogous to PDH locking but detecting incoherent fluorescence instead of transmitted light, with lock-in amplifier and servo feedback. We retrieve the clock frequency from the PDCS using  $\nu_{\text{clk}}^{\text{pdcs}} = 2(n_{-}\nu_{\text{rep}}^{\text{pdcs}} + \delta_{-} - \delta_{+}) = 2[n_{-}(\nu_{\text{IF}}^{\text{rep}} + m\nu_{\text{rf}}^{\text{rep}}) + \delta_{-} - \delta_{+}]$ , where  $\delta_{-} = \nu_{-} - \nu_0/2 = 46334200 \text{ kHz}$  and  $\delta_{+} = \nu_{+} - \nu_0 = -160092120.004 \text{ kHz}$  are the locked offsets of the two pumps from the clock input. We determine these offsets accurately by phase

locking and frequency downconversion of the pump-clock beat notes using respective EO combs (see Section S.8). We measured the repetition rate  $\nu_{\text{rep}}^{\text{pdcS}} = (737302133.41 \pm 0.05)$  kHz over seventy-five minutes, yielding  $\nu_{\text{clk}}^{\text{pdcS}} = 385284566278 \pm 26$  kHz. We retrieve the fiber comb clock frequency from  $\nu_{\text{clk}}^{\text{fiber}} = k\nu_{\text{rep}}^{\text{fiber}} + \nu_{\text{ceo}}^{\text{fiber}} + \delta_k$  with  $\delta_k = 35$  MHz the locked offset of the  $k^{\text{th}}$  comb tooth from the clock input,  $\nu_{\text{ceo}}^{\text{fiber}} = -15$  MHz,  $k = 3082212$ , and the measured  $\nu_{\text{rep}}^{\text{fiber}} = 125002.611$  kHz  $\pm 7$  mHz. This leads to  $\nu_{\text{clk}}^{\text{fiber}} = (385284566275 \pm 20)$  kHz. Compared to the published two-photon  $^{87}\text{Rb}$  transition frequency of  $(\nu_0 = 385284566370.400 \pm 10)$  kHz,<sup>30,46–50</sup> where the standard deviation represents the average across all the references, the PDCS-determined clock laser frequency exhibits an offset of  $\nu_{\text{clk}}^{\text{pdcS}} - \nu_0 = (-92 \pm 26)$  kHz and the fiber comb determined clock frequency is  $\nu_{\text{clk}}^{\text{fiber}} - \nu_0 = (-95 \pm 20)$  kHz. Hence both OFCs exhibit similar offsets, with a discrepancy from each other that is well within their respective standard deviations. The observed clock frequency offset is attributed to systematic effects in the vapor cell. Vapor density may exceed temperature-based estimates from resistance temperature detectors due to temperature gradients in the compact geometry used in this experiment.  $^{87}\text{Rb}$ – $^{87}\text{Rb}$  collisional shifts, which scale exponentially with temperature, can contribute tens of kHz of frequency shift. Atom-wall collisions likely contribute more significantly in this smaller cell than in larger cells, though these effects remain poorly characterized. Importantly, this shift does not compromise operational performance as observed in the Allan deviation in Fig. 4c.

## Data availability

The data that supports the plots within this paper and other findings of this study are available from the corresponding authors upon request.

## Acknowledgments

G.M., J.S., and K.S. acknowledge partial funding support from the Space Vehicles Directorate of the Air Force Research Laboratory and the NIST-on-a-chip and IMS programs of the National Institute of Standards and Technology. G.M., K.S., and M.E. acknowledge partial funding support from Marsden Fund of the Royal Society Te Apārangi [Grant No. 23-UOA-071]. P.S and C.M. acknowledge support from collaborative agreement 2022138-142232 and 2023200-142386 with the National Center for Manufacturing Sciences as sub-awards from US DoD cooperative agreements HQ0034-20-2-0007 and HQ0034-24-2-0001 and from NIST contract 60NANB24D106. D.J.B. acknowledges funding from the DARPA MTO Gryphon program under award number HR0011-22-2-0008. Any mention of commercial products within this article is for information only; it does not imply recommendation or endorsement by the National Institute of Standards and Technology nor the U.S. Government. Approved for public release, distribution is

unlimited. Public Affairs release approval #AFRL-2026-0416. The views expressed are those of the authors and do not reflect the official policy or position of the U.S. Government. We thank Karl D. Nelson of Honeywell Aerospace Technologies for help with fabrication of the silicon nitride coil resonator. We thank Saleha Fatema and Zachary Newman for insightful feedback.

## Author contributions

G.M., M.E., and K.S conceptualized the project. G.M., P.S., and M.E. developed the theoretical framework with help from Z.L. and C.M. G.M. designed the resonators. S-C.O. helped with initial device linear characterization. M.H., K.L. and D.J.B. designed and fabricated the integrated reference cavity. R.B, R.R. and S.K. developed the Rb atomic clock system. G.M. led the project, performed the measurements as single operator, and performed all analysis. J.S. helped with the metrology analysis. G.M., M.E., and K.S. wrote the manuscript, with input from all coauthors. All the authors contributed to and discussed the content of this paper.

## Competing interests

G.M., M.E., and K.S have submitted a provisional patent application based on aspects of the work presented in this paper. The other authors declare no competing interests.

## Supplementary Information: Self-aligned optical microcomb emerging between octave separated lasers

### Contents

S.1. Numerical investigation of self-aligned PDCSs	16
S.2. Pulley coupler chromatic dispersion	17
S.3. Impact of temperature and thermo-refractive dispersion	17
S.4. Unsynchronized PDCS repetition rate dependence with pump detuning	18
S.5. Geometry and pumped mode tolerance of the self-aligned PDCS	18
S.6. PDCS-crystal states and PDCS envelope extraction	19
S.7. Cross correlation measurement of the repetition rate	20
S.8. Complete experimental apparatus	21

### S.1. Numerical investigation of self-aligned PDCSs

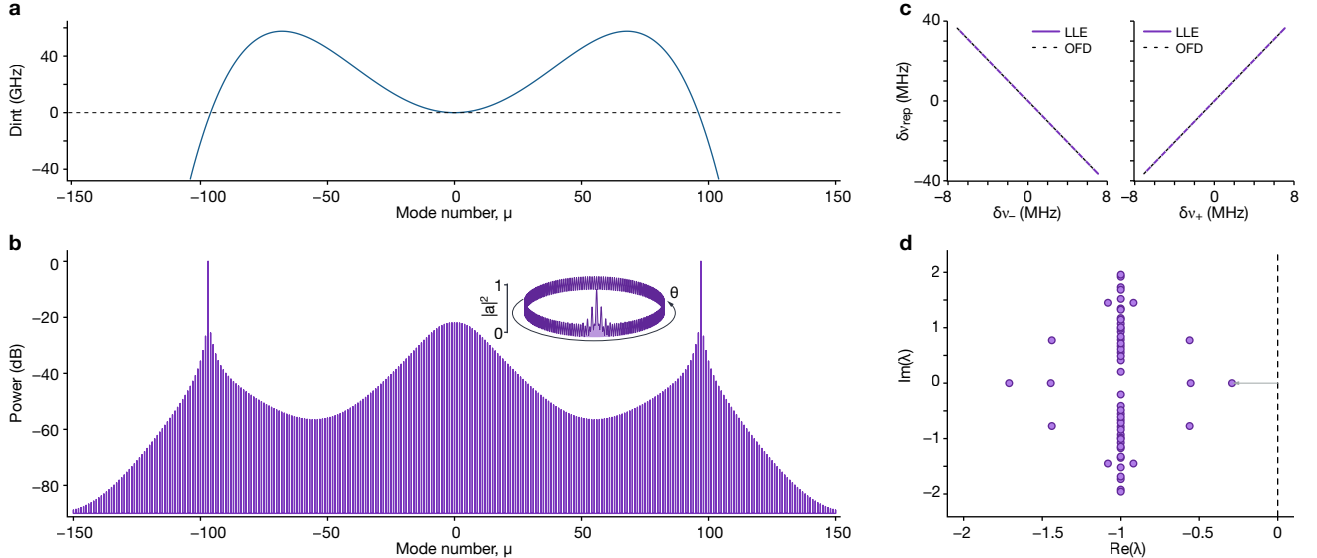


**Fig. S.1 – Numerical study of self-aligned PDCS**— **a** Integrated dispersion profile  $D_{\text{int}}(\mu)$  used in the numerical simulations where only the even order dispersion terms are considered. The dispersion is chosen such that  $D_{\text{int}}(\mu_{\pm}) \approx 0$  at the pumped modes  $\mu_{\pm} = \pm 97$ . **b** Simulated self-aligned PDCS spectrum. The intracavity field azimuthal profile is shown in the inset. **c** Repetition rate variation of the PDCS ( $\delta\nu_{\text{rep}}^{\text{pdc}}$ ) as a function of the negative (left) and positive (right) pump detuning variation  $\delta\nu_{\pm}$ . The solid lines are the simulation results and the dashed lines the expected disciplining from the optical frequency division between the two pumps. **d** Eigenvalue spectrum of the linearized operator corresponding to the self-aligned PDCS solution. The arrow represents the position-shifting eigenvalue (Goldstone mode) that has become negative, indicating the symmetry breaking, and hence synchronization the pumps.

To study numerically the generation and self-alignment of the PDCS, we use the multi-pumped Lugiato-Lefever equation (LLE).<sup>61</sup>

$$\frac{\partial a(\theta, t)}{\partial t} = -\frac{\kappa}{2}a + i \sum_{\mu} D_{\text{int}}(\mu) A(\mu) e^{i\mu\theta} + i|a|^2 a + \sqrt{\kappa_{\text{ext}} P_-} \exp \left\{ i[2\pi\delta\nu_- + 2\pi D_{\text{int}}(\mu_-)]t + i\mu_- \theta \right\} \\ + \sqrt{\kappa_{\text{ext}} P_+} \exp \left\{ i[2\pi\delta\nu_+ + 2\pi D_{\text{int}}(\mu_+)]t + i\mu_+ \theta \right\}, \quad (\text{S.1})$$

with  $a(\theta, t)$  the intracavity field profile along the resonator angle  $\theta$  and time  $t$ ,  $\kappa$  the cavity loss rate,  $D_{\text{int}}(\mu)$  the integrated dispersion computed at  $(\mu_- + \mu_+)/2$  (i.e., at the spectral center of the PDCS) and has unit of frequency (not angular frequency),  $P_{\pm}$  the negative and positive pump power,  $\delta\nu_{\pm}$  the pump detunings from their respective cavity resonances, and  $\mu_{\pm}$  the mode numbers of the pumps relative to the center of the PDCS. The other parameters are defined in the main text. We chose symmetric conditions with  $\mu_+ = -\mu_- = 97$  to ensure the integrated dispersion  $D_{\text{int}}(\mu_{\pm})$  approaches zero at the two pumped modes. We account only for even-order dispersion terms, such that  $D_{\text{int}}(\mu) \equiv (D_2/2)\mu^2 + (D_4/24)\mu^4$  (Fig. S.1a). This approach renders the integrated dispersion and OPO frequency matching condition identical.

Currently, an understanding of the full phase space of PDCSs and their various excitation pathways remains under exploration.<sup>62</sup> Therefore, we assume the single PDCS as an initial condition and allow it to evolve in time, governed by Eq. (S.1), to confirm that the PDCS is indeed a stable solution of the system. From this evolution, we extract the intracavity field profile, consisting of a single pulse with periodic modulation from the beating between the two pumps that travel at the same group and phase velocity, along with its spectrum (Fig. S.1b). To verify the self-alignment, we proceed similarly to the experiment and scan the negative pump detuning  $\delta\nu_-$  while keeping the positive pump detuning  $\delta\nu_+$  fixed, and vice versa. First, we observe that the PDCS remains stable over the range of detunings studied. Second, the PDCS repetition rate variation  $\delta\nu_{\text{rep}}^{\text{pdc}}$  changes linearly with the pump detuning variation and the modal separation between the two pumps, as expected from optical frequency division (Fig. S.1c). Finally, we study the stability of the PDCS by linearizing Eq. (S.1) around the PDCS solution and finding the eigenvalues  $\lambda$  of the linearized operator, following the approach in Ref.<sup>32</sup> and described in more detail in Refs.<sup>63,64</sup> We observe that the position-shifting eigenvalue (the Goldstone mode) becomes negative, confirming the symmetry breaking and self-alignment of the PDCS (Fig. S.1d).

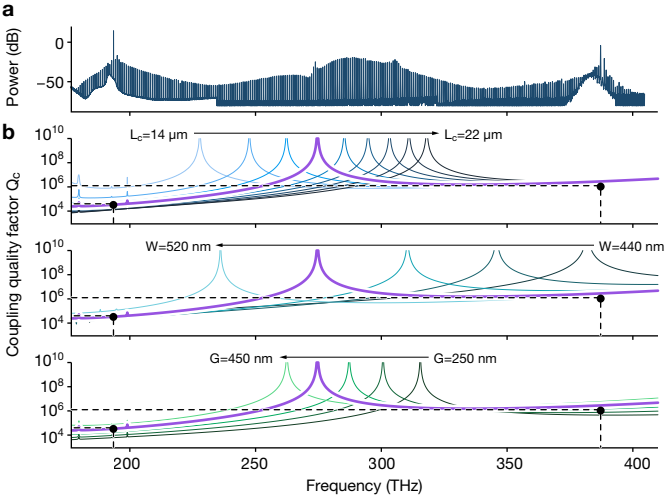


**Fig. S.2 – Pulley-coupler chromatic dispersion engineering for PDCS generation**— **a** Self-aligned PDCS spectra for  $RW = 850$  nm presented in Fig. 1. The pulley coupler characteristic of this devices, and the other  $RW$  testes in Section S.5 are  $G = 400$  nm,  $L_c = 17$   $\mu\text{m}$ , and  $W = 500$  nm, resulting in a coupling quality factor at the pump of  $Q_c(\nu_-) \simeq 40 \times 10^3$  and  $Q_c(\nu_+) \simeq 1.2 \times 10^6$ , which is overcoupled and critically-coupled respectively. **b** Finite element method simulations of the pulley coupling quality factor against the frequency for a waveguide with the nominal dimension but varying pulley length (top), varying waveguide width (center), and varying gap size (bottom). The purple trace in the three subplots correspond to the nominal design used in experiment. The dashes lines and circles correspond to the two pumps and their respective targeted coupled quality factor.

## S.2. Pulley coupler chromatic dispersion

For efficient PDCS generation and self-alignment to octave-apart pump lasers, the chromatic dispersion of the microring coupling to a bus waveguide is critical. Although optimization for lowering the degenerated-OPO threshold an optimizing the coupling in every band of interest is still a very active research topic,<sup>65,66</sup> we find that for robust self-aligned PDCS generation the two pumps must be simultaneously injected into the microring resonator with high efficiency for effective nonlinear interaction, while providing sufficient frequency tunability to satisfy both the OPO condition and the self-alignment frequency offset condition. To achieve this, we design the bus waveguide to couple to the microring resonator in a pulley-like configuration, which exploits the phase mismatch between the bus and the microring resonator to engineer the chromatic dispersion of the coupling quality factor  $Q_c$ . In all devices tested in this manuscript that yield a self-aligned PDCS (see Section S.5), the pulley coupler consists of a bus waveguide (with  $\text{Si}_3\text{N}_4$  thickness equal to that of the ring) with a width of  $W = 500$  nm, wrapped around the ring over a pulley length of  $L_c = 17$   $\mu\text{m}$ , and separated by a gap of  $G = 400$  nm. This coupler enables over-coupling at the  $\nu_-$  pump while maintaining critical coupling at the  $\nu_+$  pump, providing greater flexibility in PDCS generation and self-alignment while remaining efficient and allowing for on-chip pump powers approaching or below one hundred milliwatt. We note that our two pumps are an octave apart, making the pulley coupler extremely robust against fabrication uncertainty. One can first assume that the pulley length remains relatively accurately fabricated. A variation of waveguide width of  $\pm 20$  nm results in the same coupling regime at both pumps, while gap variation has limited impact on the coupling (Fig. S.2).

## S.3. Impact of temperature and thermo-refractive dispersion

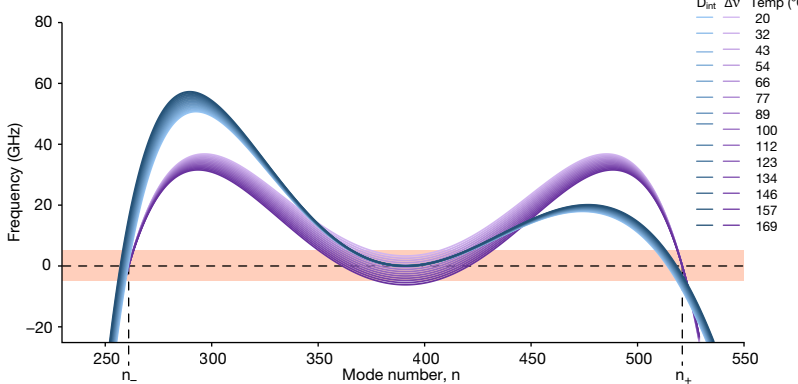


**Fig. S.3 – Temperature dependence of phase matching for PDCS generation and self-alignment**— Using finite-element method (FEM) simulations, we compute the OPO frequency mismatch  $\Delta\nu$  (varying purple shades) and the integrated dispersion at the PDCS spectral center  $D_{\text{int}}$  (varying blue shades) as a function of resonator temperature. The increase of temperature, happening due to residual absorption of the pumps, leads to a negative shift in  $\Delta\nu$ , enabling phase-matching for PDCS generation. However, the integrated dispersion  $D_{\text{int}}$  does not change significantly, enabling the PDCS to remain self-aligned over the temperature range studied.

Here, we discuss the impact of resonator temperature on PDCS generation and self-alignment. As with standard DKSs, the on-chip pump powers and residual absorption of the  $\text{Si}_3\text{N}_4$  resonator increase the resonator temperature. Although thermal bistability is generally a detriment for stably accessing DKS states with a single pump laser, it does not hinder PDCS generation and self-alignment. In particular, we do not implement frequency sweeping faster than the thermal lifetime to counter thermal bistability. Although the system is dual-pumped, we do not believe it

operates in an identical fashion to laser-cooling and thermo-optic stabilization of microresonators that enable easier DKS access.<sup>40,41</sup> Indeed, the negative pump is very largely over-coupled, so its contribution to the thermal load is minimal compared to the positive pump, and no backaction mechanism stabilizes the resonator temperature. However, the positive pump is critically coupled and operated near visible wavelengths where  $\text{Si}_3\text{N}_4$  absorption is larger, leading to a significant thermal load that red-shifts the resonator modes. In addition, the large frequency span of interest here (from 1550 nm to 775 nm) means that the mode overlap between the  $\text{Si}_3\text{N}_4$  microring resonator core and the  $\text{SiO}_2$  cladding—two materials with different thermo-refractive coefficients—varies significantly with wavelength, leading to effective thermo-refractive chromatic dispersion. We numerically model the impact of temperature change from room temperature (20 °C) to 169 °C on the resonator dispersion using finite-element method (FEM) simulations, extracting the integrated dispersion at the PDCS spectral center  $D_{\text{int}}$  and the OPO frequency mismatch  $\Delta\nu$  [Fig. S.3]. We observe the behavior of  $\Delta\nu$  close to the degenerate-OPO mode  $(n_- + n_+)/2$ , and find that it starts at positive values at room temperature and becomes smaller with increased temperature, eventually crossing zero and becoming negative. This indicates that the OPO condition shifts slightly between the cold cavity during linear measurements and the hot cavity when laser pumps are injected. This shift explains the slight positive offset of the OPO conditions for the device of interest (Fig. 2a and Fig. S.5). Importantly, within the temperature range studied,  $D_{\text{int}}$  does not change significantly, and the two pumps remain close to a working point of  $D_{\text{int}}(M_{\pm}) \approx 0$ , enabling the PDCS to become self-aligned.

One important note is that the over-coupling of the pump resonances in the  $\nu_-$  band, and the resulting large linewidths, enables large frequency tuning of the OPO and self-alignment conditions. This makes self-aligned PDCS generation robust in overcoming both fabrication-induced offsets from the target geometry and undesirable thermal effects that might otherwise be a limitation.

#### S.4. Unsynchronized PDCS repetition rate dependence with pump detuning

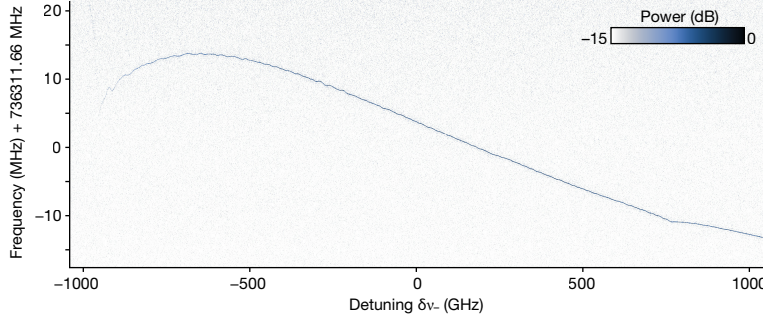


**Fig. S.4 – Repetition rate dependence on the negative pump of the unsynchronized PDCS—** Repetition rate spectrogram of the unsynchronized PDCS as a function of the negative pump detuning variation ( $\delta\nu_-$ ) across more than 2 GHz.

Although we focus the main text on the self-aligned PDCS, we also study the repetition rate dependence of an unsynchronized PDCS with respect to negative pump detuning variation  $\delta\nu_-$ . In this regime, the repetition rate variation  $\delta\nu_{\text{rep}}^{\text{pdc}s}$  is not expected to follow the optical frequency division relation because the PDCS is not synchronized to the pumps. We observe that the repetition rate  $\nu_{\text{rep}}^{\text{pdc}s}$  increases as  $\delta\nu_-$  decreases (Fig. S.4), opposite to the self-aligned PDCS case (see Fig. 2). Further work is underway to understand this behavior. We probe the unsynchronized PDCS over a detuning range exceeding 2 GHz and limit the range only to ensure PDCS stability during measurement. This flexibility and robustness against negative pump detuning stems directly from the over-coupling regime of the negative pump resonance, which exhibits a linewidth of nearly 5 GHz. We note that the PDCS repetition rate exhibits a turning point near  $\delta\nu_- \approx -600$  Hz, which may prove valuable for future low-noise microwave generation applications and pump noise rejection.

#### S.5. Geometry and pumped mode tolerance of the self-aligned PDCS

A critical aspect of our self-aligned PDCS platform is its compatibility with foundry fabrication processes. Although foundry-fabricated devices exhibit high quality, they still contain fabrication imperfections that cause deviations from intended design parameters. Therefore, resilience to fabrication imperfections constitutes a critical criterion for deployable integrated OFC platforms. To assess this resilience, we investigate multiple devices fabricated during the same run. We observe that all devices with similar geometry—ring widths from  $RW = 840$  nm to  $RW = 860$  nm, corresponding to approximately 3 % variation—produce quasi-harmonic self-aligned PDCS with the correct dispersion condition (Fig. S.5a-c). We implemented additional ring widths in the same fabrication run, but the limited span available for the positive pump (due to the taper amplifier gain bandwidth) prevented testing of all devices. In addition, all three tested devices exhibited excellent tolerance against pump mode variation (Fig. S.5d), which was again limited only by the available pump laser wavelength range. An important contribution to this large tolerance

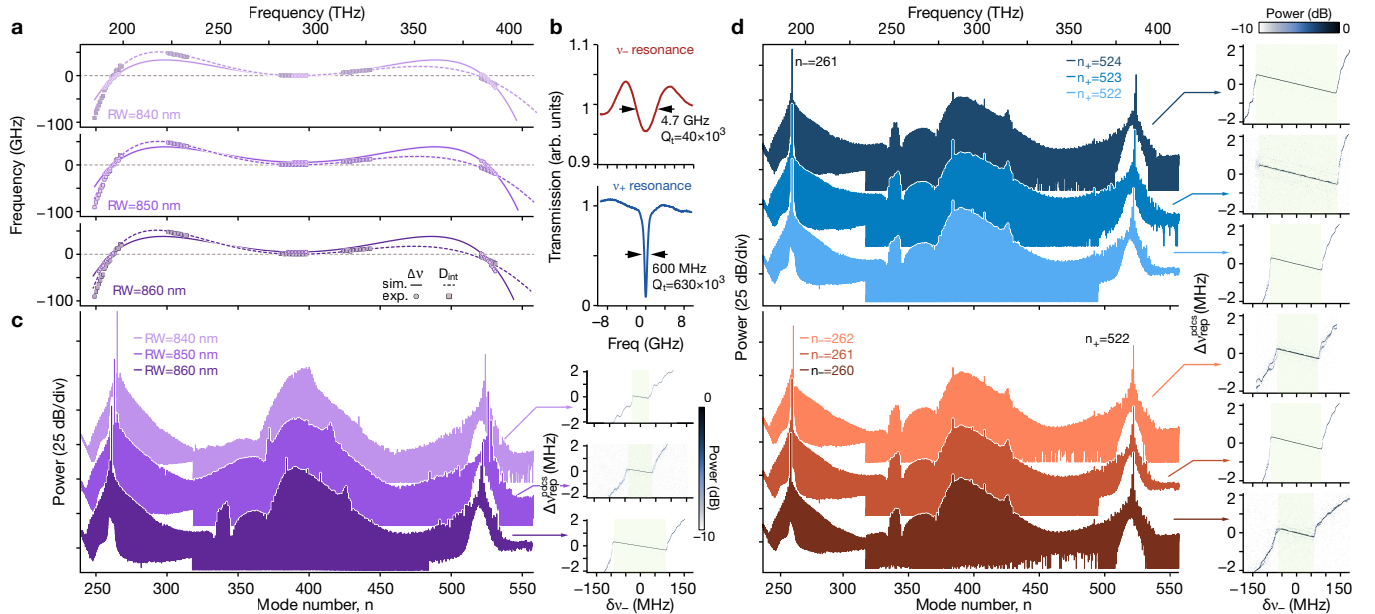


**Fig. S.5 – Fabrication imperfection resilience and pumped mode versatility**—**a** Integrated dispersion  $D_{\text{int}}$  (dashed) and OPO frequency mismatch  $\Delta\nu$  (solid) for three different devices with slightly different ring widths (840 nm, 850 nm, and 860 nm) with experimental data (markers) in agreement with simulation (lines). **b** Measured pumped resonance spectra for the 860 nm ring width device. The negative pump resonance is strongly overcoupled, with a loaded quality factor  $Q_t \approx 40 \times 10^3$ , while the positive pump resonance is nearly critically coupled, with  $Q_t \approx 640 \times 10^3$ . The overcoupling of the negative pump resonance enables large detuning tolerance for PDCS generation and self-alignment. **c** Measured PDCS spectra for the three different devices when pumping at harmonic modes. **d** Measured PDCS spectra for the 860 nm ring width device pumped at different modes for both the positive (top) and negative (bottom) pumps. All the spectrograms shown to the right of the PDCS spectra in (c)-(d) show self-alignment through disciplining of the repetition rate variation  $\Delta\nu_{\text{rep}}^{\text{pdcsp}}$  against the negative pump detuning  $\delta\nu_-$ .

is the chromatic dispersion of the coupling using the pulley coupler,<sup>39</sup> which critically couples the positive pump for efficient power transfer to the cavity and leverages a large effective nonlinear coefficient at short wavelengths,<sup>67</sup> while over-coupling the negative pump (Fig. S.5b). The latter is crucial because it allows the PDCS to exist over a very large negative pump frequency detuning, enabling the system to overcome fabrication imperfections, frequency mismatch, and dispersion offset.

## S.6. PDCS-crystal states and PDCS envelope extraction

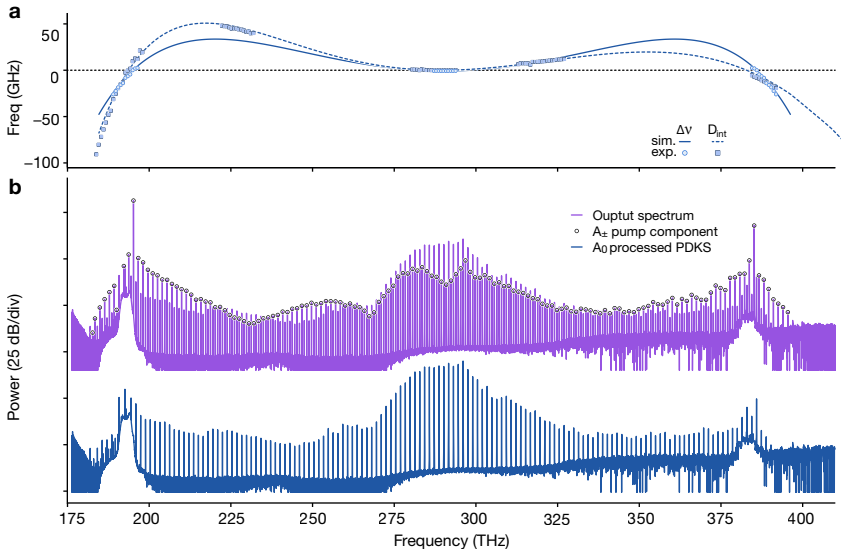


**Fig. S.6 – PDCS crystal for post-processing out pump components**—**a** Integrated dispersion  $D_{\text{int}}$  (dashed) and OPO frequency mismatch  $\Delta\nu$  (solid) for a device with 840 nm ring width. **b** Under appropriate pump conditions, determined primarily by pump power, a two-PDCS-crystal structure emerges (top purple). In such a scenario, the PDCS crystal and the microcomb generated by cross-phase modulation around the pumps are offset by one mode, in addition to being slightly offset from one another outside the self-alignment region. This configuration enables straightforward extraction of the pump microcomb (top markers), which can be subtracted from the total spectrum to retrieve the PDCS envelope (bottom blue). This procedure reveals the PDCS dispersive wave previously obscured by the pump microcombs and confirms alignment with the phase-matching condition predicted by  $D_{\text{int}}$ .

Experimentally, we find that our octave-spanning PDCS, under appropriate pump conditions, which we find empirically to be primarily determined by the pump powers, can emerge as a crystal state, where multiple PDCSs are

equally azimuthally spaced within the microring resonator [Fig. S.6]. In particular, we generate a 2-PDCS-crystal state using the 840 nm ring width device by pumping at modes  $n_- = 265$  and  $n_+ = 523$  (*i.e.*, 195.2 THz and 385.2 THz). Since each PDCS can exist with either a 0 or  $\pi$  phase,<sup>5,6</sup> we repeat the experiment until the two PDCS are both in phase, observable through a bright peak at  $n_0 = (n_- + n_+)/2$ . However, since  $n_0 - n_- = n_+ - n_0$  is odd, the two pumps are spectrally placed at dark teeth of the PDCS crystal spectrum. This configuration enables straightforward extraction of the pump microcomb spectrum by selecting every other tooth from the total spectrum (top spectrum and markers in Fig. S.6b). This post-processing capability reveals spectral features previously hidden by the pump microcombs, most notably the PDCS dispersive wave. The extracted dispersive wave frequency aligns precisely with the phase-matching condition predicted by the integrated dispersion  $D_{\text{int}}$  (Fig. S.6a), confirming the theoretical understanding of PDCS generation. Beyond fundamental interest, this ability to separate PDCS and pump-generated spectral components through crystal-state engineering provides an additional degree of freedom for tailoring the output spectrum for specific applications, particularly where isolated PDCS spectral coverage is desired without pump laser contributions.

### S.7. Cross correlation measurement of the repetition rate

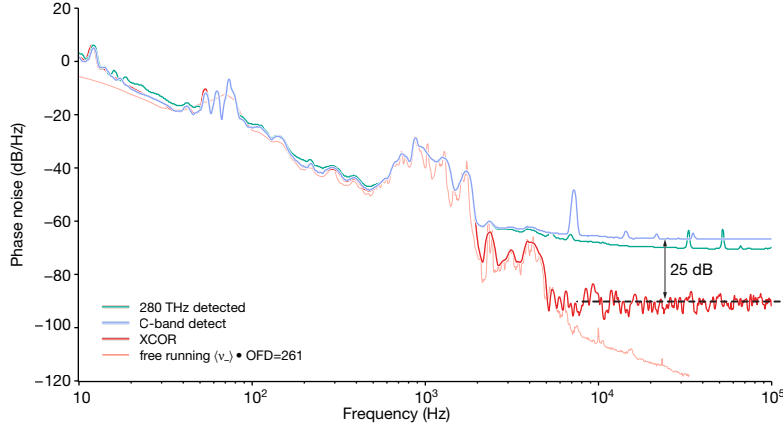


**Fig. S.7 – Cross-correlation measurement of PDCS repetition rate**— PDCS Repetition rate phase noise power spectral density with and without cross-correlation (XCOR). Here the positive pump locks the CEO and the negative pump runs freely; hence the repetition rate follows OFD of the latter's noise (pink). When frequency downconverting  $\nu_{\text{rep}}^{\text{pdc}}$  with a single EOPM apparatus (*i.e.*, an EO comb), its noise limits detection beyond 2 kHz. By measuring the repetition rate in both the C-band (blue) and at the center of the PDKS around 280 THz (teal) with independent EO combs, we perform an XCOR measurement where each EO comb downconverter acts as an input to the phase noise analyzer. This rejects the uncorrelated EO comb noise and lowers the noise floor by approximately 25 dB (red).

With the repetition rate of the PDCS  $\nu_{\text{rep}}^{\text{pdc}}$  being in the 730 GHz range, we cannot directly detect it through photodetection of two adjacent comb teeth. Instead, as discussed in the Methods, we use an electro-optic phase modulation (EOPM) apparatus, also known as an electro-optic comb (EO comb), that acts as a local oscillator to down-convert the PDCS repetition rate to a detectable frequency  $\nu_{\text{IF}}^{\text{rep}} = \nu_{\text{rep}}^{\text{pdc}} - m\nu_{\text{rf}}^{\text{rep}}$ . Therefore, the phase noise power spectral density that we measure is such that  $\langle \nu_{\text{IF}}^{\text{rep}} \rangle = \langle \nu_{\text{rep}}^{\text{pdc}} \rangle + m\langle \nu_{\text{rf}}^{\text{rep}} \rangle$ . Hence, as in any frequency down-conversion scheme, the local oscillator phase noise  $m\langle \nu_{\text{rf}}^{\text{rep}} \rangle$  adds to the measured phase noise of the PDCS repetition rate. Although high-quality microwave sources are available, the multiplication factor  $m$  from the number of EO sidebands needed to span two adjacent PDCS teeth is large ( $m \approx 42$  here). Therefore, this produces a high noise floor, particularly for Fourier frequencies above 2 kHz (Fig. S.7).

A method to overcome this EO comb noise floor limitation is to use the two input channels of the phase-noise analyzer (PNA) to perform a cross-correlation (XCOR) measurement. In such a scheme, the device under test (DUT) is measured in two independent ways, so that the uncorrelated noise from the two DUT inputs is rejected. Therefore, by frequency down-converting  $\nu_{\text{rep}}^{\text{pdc}}$  using two independent EO combs, their uncorrelated noise will be rejected, leaving only the PDCS repetition rate phase noise. We implement such a scheme using the large spectral span of the PDCS and measuring the repetition rate around 280 THz (*i.e.*, close to the PDCS center) and in the C-band, two modes away from the negative pump (see Fig. S.8). Using this technique, the phase noise PSD  $\langle \nu_{\text{IF}}^{\text{rep}} \rangle$  from both EO comb detections shows the same profile, confirming the same repetition rate throughout the PDCS spectrum. Using these two as the DUT inputs of the PNA, we show a reduction of about 25 dB with respect to the single EO comb-limited noise floor, enabling more accurate measurement. The limitation in further noise floor reduction comes from the limited averaging available in the XCOR measurement. Indeed, the frequency drift, even when locked to the reference cavity (as seen in the Allan deviation in Fig. 4c), limits the total averaging time to about 5 min before the frequency drift prevents proper correlation between the two channels and better averaging. However, the currently observed reduction in the noise floor is sufficient to demonstrate the optical frequency division in all the locking regimes studied.

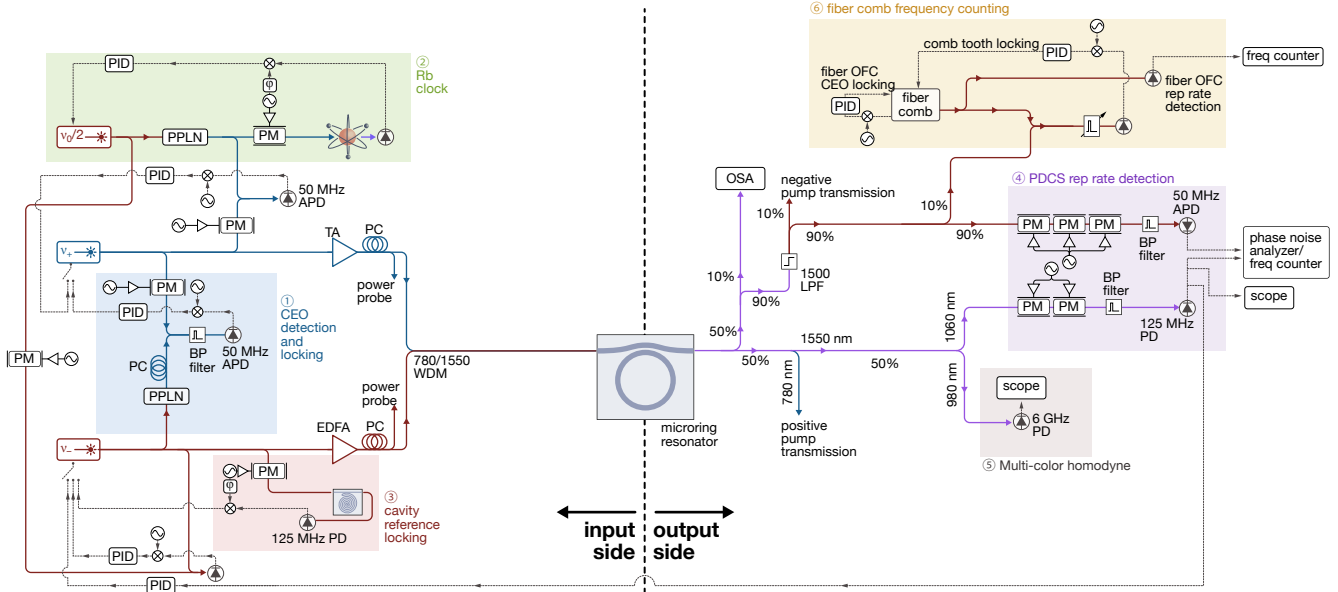


**Fig. S.8 – Complete experimental setup**—Complete experimental apparatus used to generate, self-align, and characterize the PDCS. The input side (left) is comprised of the two pumps lasers  $\nu_-$  and  $\nu_+$ , amplified by a TA and an EDFA, respectively, that are sent into the microring resonator. Each laser is tapped for setting and stabilizing the CEO of the subsequently generated PDCS comb (blue block ①), locking the lasers to the Rb clock (green block ②), or locking the negative pump to the reference cavity (red block ③). The output side (right) is solely used to characterize the PDCS, with the exception of the self-stabilized microwave-to-optical link case, where the repetition rate detection (purple block ④) is fed back to the negative pump laser to lock it, and cannot be done otherwise. The fiber comb (yellow block ⑤) is used to measure the absolute frequency of the PDCS comb teeth. The multicolor homodyne to detect  $\Delta\nu_{\text{ceo}}$  is displayed in the gray block ⑥. PC: polarization controller; TA: tapered amplifier; EDFA: erbium-doped fiber amplifier; WDM: wavelength-division multiplexer; OSA: optical spectrum analyzer; PM: electro-optic phase modulator; LPF: long-pass filter; BPF: band-pass filter; PD: photodetector; APD: avalanche photodetector; PID: proportional-integral-derivative controller; PPLN: periodically-poled lithium niobate waveguide;

### S.8. Complete experimental apparatus

The complete experimental apparatus used in this work is shown in Fig. S.8. In our self-aligned PDCS system, both pumps generate and trigger the synchronization of the cavity soliton, thereby becoming comb teeth. The independent locking of the two pumps on the input side enables stabilization *before PDCS generation*, except in the microwave-to-optical coherent link case, where self-stabilization requires that the detected repetition rate  $\nu_{\text{rep}}^{\text{PDCS}}$  be fed back for locking.

Thus, we detect the heterodyne between the doubled negative pump  $\nu_-$  and the positive pump  $\nu_+$  to lock what will become the CEO frequency  $\nu_{\text{ceo}}^{\text{PDCS}}$  once the PDKS is generated (Fig. S.8, block ①). We note that since the CEO detection occurs *before* the chip, the power available exceeds any on-chip light generated (either by the PDCS or any other DKS). Therefore, we do not require amplification of the negative pump laser while using a commercial fiber-pigtailed periodically poled lithium niobate (PPLN) crystal and still obtain a doubled power  $P_{2\nu_-} \approx 10 \mu\text{W}$ , which we beat against a phase-modulated tap of the positive pump, at a power  $P_{\nu_+} \approx 1 \text{ mW}$ . As described in the Methods section,  $\nu_{\text{ceo}}^{\text{PDCS}}$  lies beyond our detectable microwave range, and thus the phase-modulation of the tapped pump is done in the overdriven regime, resulting in an electro-optic comb for frequency downconversion. The frequency downconverted CEO  $\nu_{\text{IF}}^{\text{ceo}}$  is then phase-locked to the 10 MHz microwave reference by feedback on one of the lasers, which in Fig. S.8 is the positive laser. Alternatively, the input laser can be locked to the Rb clock laser (Fig. S.8, block ②) where a CW laser is doubled and locked to the  $5S_{1/2}-5D_{5/2}$  two-photon transition of the  $^{87}\text{Rb}$  vapor, which is set in a 100 °C gas cell. The clock laser is phase (frequency) modulated and sent through the vapor cell, similar to a Pound-Drever-Hall (PDH) technique. The atoms are preferentially excited by resonant light, and fluoresce as they relax back to the  $5S_{1/2}$  state. We detect the power of this fluorescence. We deliberately phase modulate the laser slower than the atomic relaxation rate in order to keep a good contrast on the detected signal. The difference from a standard PDH approach is that the power of the fluorescence (incoherent) is detected instead of the probe laser power, and that there are therefore no off-resonance sidebands for the signal to interfere with. From there it's the same control loop as a PDH, with lock-in and servo feedback. The fundamental and second harmonic of this laser are then used to lock the negative and positive pump lasers, respectively, using heterodyne detection and feedback on each laser current. Finally, the positive pump can be locked to a high-finesse reference cavity (Fig. S.8, block ③) using PDH locking.

The output of the experimental setup is dedicated to the characterization of the PDCS. A portion is extracted to probe the PDCS spectrum using an optical spectrum analyzer (OSA). Another portion is sent to the repetition rate detection block (Fig. S.8, block ④), using appropriate wavelength demultiplexers (WDMs) to select the desired spectral region for  $\nu_{\text{rep}}^{\text{PDCS}}$  detection. EO combs at 1550 nm (190 THz) and 1060 nm (280 THz), consisting of two and three phase modulators respectively, down-convert the PDCS repetition rate to obtain two  $\nu_{\text{IF}}^{\text{rep}}$  signals. In the case of self-stabilization for a microwave-to-optical link, the 1060 nm-detected  $\nu_{\text{IF}}^{\text{rep}}$  provides feedback to the pump laser to lock the PDCS repetition rate to the 10 MHz reference. In the optical-to-microwave link case, the two detected  $\nu_{\text{IF}}^{\text{rep}}$  are used for the XCOR measurement to reject the EO comb noise floor, as discussed in Section S.7. To characterize the optical frequency of the PDCS comb teeth, a portion of the PDCS output is heterodyned against a fiber comb whose CEO is locked to the 10 MHz reference and whose repetition rate is locked to a given PDCS comb tooth. This configuration enables precise optical frequency counting from the optical frequency division operation of the fiber comb. Finally, a portion of the PDCS is extracted around 980 nm (*i.e.* 305 THz) to monitor the multi-color beat  $\Delta\nu_{\text{ceo}}$  between the PDCS and the pump comb components, which vanishes when the PDCS becomes self-aligned.